1973

# Fatigue crack propagation behavior of the unidirectionally solidified ni-ni3nb eutectic composite

William J. Mills
*Lehigh University*

# FATIGUE CRACK PROPAGATION BEHAVIOR OF THE UNIDIRECTIONALLY SOLIDIFIED Ni-$Ni_3Nb$ EUTECTIC COMPOSITE

by

William J. Mills

A Thesis

Presented to the Graduate Faculty

of Lehigh University

in Candidacy for the Degree of

Master of Science

in

Metallurgy and Materials Science

Lehigh University

1973

This thesis is accepted and approved in partial fulfillment of the requirements for the degree of Master of Science.

August 13 1973
(date)

Professor in Charge

G. P. Cavard 31 Aug '73
Chairman of Department

## ACKNOWLEDGEMENT

The author wishes to gratefully acknowledge the guidance of his advisor Professor Richard W. Hertzberg. Sincere appreciation is also expressed to Professor R. Wayne Kraft and Professor Michael R. Notis for their helpful suggestions and advice.

Gratitude is also extended to the senior staff and to fellow graduate students for their constant cooperation and assistance with special thanks to Keith Hill and Richard Gangloff for their enlightening discussions during this research program. In addition, the assistance of the machine shop, the secretarial staff and the technicians at Coxe and Whitaker Laboratories was greatly appreciated. The author wishes to acknowledge the Bell Telephone Laboratories and the Western Electric Company in Allentown, Pa. who graciously performed the machining of the samples employed during the current investigation.

Finally, the author also gratefully acknowledges the financial support of the National Aeronautics and Space Administration under Grant NGR-39-007-007.

# TABLE OF CONTENTS


| | Page |
|---|---|
| TITLE PAGE | |
| CERTIFICATE OF APPROVAL | ii |
| ACKNOWLEDGEMENT | iii |
| TABLE OF CONTENTS | iv |
| LIST OF FIGURES | vii |
| ABSTRACT | 1 |
| CHAPTER I - INTRODUCTION | 3 |
| 1.1 Introduction to Fiber Reinforced Eutectic Composites | 3 |
| 1.2 The Ni-$Ni_3Nb$ Eutectic System - A Review | 5 |
| 1.2.1 Morphology | 5 |
| 1.2.2 Mechanical Properties and Deformation Mechanisms | 6 |
| 1.3 Fatigue Behavior of Eutectic Composites - A Review | 7 |
| 1.3.1 Binary Eutectic Systems | 7 |
| 1.3.2 The Ni-$Ni_3Nb$ System | 9 |
| 1.4 Objective of the Current Investigation | 11 |
| CHAPTER II - THE AGE HARDENING BEHAVIOR OF THE CONTROLLED Ni-$Ni_3Nb$ COMPOSITE | 13 |
| 2.1 Introduction | 13 |
| 2.2 Presentation and Discussion of Results | 15 |
| 2.2.1 Microstructure | 15 |
| 2.2.2 Micro-Hardness Results | 17 |

TABLE OF CONTENTS (cont'd.)


| | | Page |
|---|---|---|
| CHAPTER III - | FATIGUE CRACK PROPAGATION IN THE Ni-$Ni_3Nb$ COMPOSITE: A FRACTURE MECHANICS APPROACH | 19 |
| 3.1 | Introduction | 19 |
| 3.2 | Fatigue Testing | 20 |
| 3.2.1 | Test Sample | 20 |
| 3.2.2 | Four-Point Bending Fatigue Apparatus | 20 |
| 3.2.3 | Test Specimen and Loading Fixture Design Verification | 21 |
| 3.3 | Presentation and Discussion of Results | 22 |
| 3.3.1 | FCP in the Unidirectional Solidified Ni-$Ni_3Nb$ Composite | 22 |
| 3.3.2 | Effect of Test Variables on FCP | 23 |
| 3.3.3 | Effect of Metallurgical Variables on FCP | 24 |
| CHAPTER IV - | FATIGUE FRACTURE SURFACE APPEARANCE | 26 |
| 4.1 | Introduction | 26 |
| 4.2 | Fractographic Observations | 29 |
| 4.2.1 | High FCP Rates: (Greater than $1.5 \times 10^{-5}$ in/cyc) | 29 |
| 4.2.2 | Low FCP Rates: (Below $5 \times 10^{-6}$ in/cyc) | 31 |
| 4.2.3 | Fracture Mechanism Transition: ($5 \times 10^{-6}$ in/cyc - $1.5 \times 10^{-5}$ in/cyc.) | 33 |
| 4.3 | Metallographic Observations | 34 |
| CHAPTER V - | CONCLUSIONS | 36 |
| TABLE I - | Data Obtained from Quantitative Metallography of U.D.S. Ni-$Ni_3Nb$ Specimens | 38 |
| TABLE II - | Data Obtained from Micro-Hardness Testing of U.D.S. Ni-$Ni_3Nb$ Specimens | 39 |

TABLE OF CONTENTS (cont'd.)


| | Page |
|---|---|
| REFERENCES | 59 |
| APPENDIX I: EXPERIMENTAL PROCEDURES | 64 |
| Solidification | 64 |
| Heat Treatment | 65 |
| Metallographic Techniques | 66 |
| Electron Microscopy Techniques | 67 |
| Micro-Hardness Testing | 69 |
| VITA | 71 |

## LIST OF FIGURES


| | | Page |
|---|---|---|
| Figure 1 | - Ni-Nb equilibrium phase diagram; Ni end (19). | 40 |
| Figure 2 | - Photomicrographs of as-grown structure.<br>(a) Cellular precipitation within a large proeutectic dendrite present in a Ni-rich ingot. 725X. (Interference Microscope)<br>(b) Aligned lamellar microstructure illustrating the absence of δ phase precipitation in on-composition ingots. 533X. | 41 |
| Figure 3 | - Photomicrographs illustrating δ phase precipitation of Widmanstatten morphology present after heat treatment.<br>(a) Aged for 3 hours at 1000°C. 200X.<br>(b) Solution treated, quenched, and aged for 1 hour at 1000°C. 533X. (Polarized Light) | 41 |
| Figure 4 | - Four-point bending test sample. | 42 |
| Figure 5 | - A photograph showing the four-point bending fixture and test sample taken during an actual fatigue test. 1/2X. | 42 |
| Figure 6 | - Fatigue crack growth rate vs $\Delta K$ for T-1 steel as compared to previously determined results (data band: 33,34). | 43 |
| Figure 7 | - Diagram depicting the plastic zone size that exists ahead of the advancing crack tip. | 44 |
| Figure 8 | - Plot of the geometrical correction factor, Y, as a function of a/W. (35) | 45 |
| Figure 9 | - Fatigue crack growth rate vs $\Delta K$ for T-1 steel corrected for plasticity. | 46 |
| Figure 10 | - Fatigue crack growth rate vs $\Delta K$ for the Ni-$Ni_3Nb$ eutectic composite ($R \leq 0.1$). | 47 |
| Figure 11 | - Fatigue crack propagation rates vs $\Delta K$ for the Ni-$Ni_3Nb$ eutectic composite ($R=0.5$). Data band represents $R \leq 0.1$ data range from Figure 10. | 48 |

## LIST OF FIGURES (cont'd.)


| | | Page |
|---|---|---|
| **Figure 12 -** | **Fatigue crack growth rate vs ΔK for the** $Ni-Ni_3Nb$ eutectic composite in a water environment. Data band represents data range in an air atmosphere taken from Figure 10. | 49 |
| **Figure 13 -** | **Fatigue crack growth rate vs ΔK for the non-**controlled alloy. Data band represents the data range for the as-controlled composite. | 50 |
| **Figure 14 -** | Fatigue crack growth rate vs ΔK for the age hardened $Ni-Ni_3Nb$ eutectic composite. Data band represents the data range for the as-grown composite. | 51 |
| **Figure 15 -** | Electron fractographs revealing the fracture surface appearance under high ΔK conditions.<br>(a) Typical striations found on the γ matrix fracture surface. 5300X.<br>(b) Striations remain parallel to the γ/δ interface irrespective of the δ platelet orientation. 6600X. | 52 |
| **Figure 16 -** | Plot representing the macroscopic (data band) and microscopic (striation spacing) growth rates of the $Ni-Ni_3Nb$ eutectic composite as a function of ΔK. The solid boxes represent the spacing of the parallel fracture markings found superimposed on the Stage I fracture surface. Boxes labelled 1-1*, 2-2* and 3-3* correspond to the spacing of the parallel fracture markings and the striations, respectively, observed on a given replica. | 53 |
| **Figure 17 -** | Electron fractographs of the fracture surface revealing:<br>(a) Twin related steps and tongues found at the δ fracture surface. 9000X.<br>(b) A fin along the interphase boundary indicative of delamination. 6600X. | 54 |
| **Figure 18 -** | Typical electron fractograph of the low growth rate region showing faceting of the γ matrix-stereographic pair. (±3°) 6600X. | 55 |

## LIST OF FIGURES (cont'd.)


| | | Page |
|---|---|---|
| **Figure 19 -** | Electron fractographs revealing the fracture surface appearance under low $\Delta K$ conditions. (a) Stage I facets on the $\gamma$ fracture surface. 6600X. (b) Stage I faceting and dark fins present at the interphase boundary indicative of delamination. 5300X. | 55 |
| **Figure 20 -** | Electron fractographs revealing parallel fracture markings. (a) Evidence of fine parallel lines superimposed on the $\gamma$ matrix faceted fracture surface. 10,000X. (b) Increased magnification of a region containing parallel fracture marking in order to resolve individual lines. (Spacing approximately 600Å) 23,000X. | 56 |
| **Figure 21 -** | Typical electron fractographs of the intermediate growth rate region illustrating: (a) Poorly defined facets and striations present in the same $\gamma$ phase region. 5600X. (b) Evidence of serpentine glide on the $\gamma$ matrix fracture surface. 14,000X. | 56 |
| **Figure 22 -** | Typical metallographic profile of a fatigue fracture at high growth rates. (Etchant B) (a) $\{211\}_\delta$ twinning and subsequent twin boundary cracking near the fracture surface. 533X. (b) $\{211\}_\delta$ and $\{011\}_\delta$ twinning, the latter appearing approximately parallel to the $\gamma/\delta$ interface. 800X. | 57 |
| **Figure 23 -** | Typical metallographic profile of a fatigue fracture at low growth rates. (Etchant A) (a) Secondary fatigue cracks that propagated parallel to the primary fatigue crack. 133X. (b) Increased magnification of the region at the secondary crack tip where a significant number of $\delta$ platelets have undergone twin boundary cracking in advance of the crack front. 533X. | 57 |

LIST OF FIGURES (cont'd.)


| | Page |
|---|---|
| Figure 24 - Schematic diagram of unidirectional solidification apparatus. | 58 |

## ABSTRACT

Room temperature four-point-bending fatigue studies of the unidirectionally solidified Ni-$Ni_3Nb$ eutectic composite have been conducted to better understand fatigue behavior in composite materials. Also, the microstructure and mechanical properties of the aligned Ni-$Ni_3Nb$ eutectic were examined in the as-grown, quenched and aged condition.

The as-grown lamellar microstructure consisted of approximately 32 volume percent $Ni_3Nb$ ($\delta$) phase, was free of $\delta$ phase precipitation, and revealed only a very low density of Widmanstatten $\delta$ precipitate after aging treatments of 3 and 10 hours at 1000°C. Properly solution treated and aged microstructure did contain a high density of $\delta$ phase precipitation of Widmanstatten morphology on $\{111\}_\gamma$ habit planes. The micro-hardness of the composite after various thermal histories was found to be a function of the total amount of $\delta$ phase present.

Fatigue crack propagation (FCP) data are reported for this eutectic composite alloy and correlated with the stress intensity factor range prevailing at the advancing crack tip. This application of fracture mechanics concepts to FCP data represents the first such reported information of its kind for eutectic composites. A power relationship between the crack growth rate and the stress intensity factor range was found to exist over a range of growth rates from $10^{-7}$ in/cyc to $10^{-4}$ in/cyc and revealed the

material to behave in a manner similar to that of medium and high strength steel alloys. As expected, only a small shift to higher crack growth rates was observed as a result of higher mean stress intensity levels, while the stress intensity range was found to be the major stress variable controlling fatigue crack propagation response. Fatigue behavior of this composite alloy was found to be sensitive to solidification and thermal history.

Metallographic examination of the fatigue fracture and electron fractographic examination of carbon-platinum replicas revealed the fatigue crack propagation mechanism to be a function of the prevailing stress intensity factor at the crack tip with a fatigue fracture mechanism transition occurring between $5 \times 10^{-6}$ in/cyc and $1.5 \times 10^{-5}$ in/cyc. At low growth rates, the Ni($\delta$) phase exhibited faceting and a general appearance reminiscent of Stage I propagation along active slip planes. Above $5 \times 10^{-6}$ in/cyc, the $\gamma$ fracture surface was characterized by the presence of fatigue striations which lay parallel to the Ni/$Ni_3Nb$ interface. The microscopic advance of the crack front--fatigue striation spacings--was found to be in excellent agreement with the macroscopic fatigue crack growth rate. At both high and low growth rates, the fatigue response of the Ni-$Ni_3Nb$ composite was controlled by the $\gamma$ matrix.

# CHAPTER I

# INTRODUCTION

## 1.1 Introduction to Fiber Reinforced Eutectic Composites

Fiber reinforced composites show great potential as high strength and high elastic modulus materials. Most composites are made by manufacturing the two components separately and then combining them with the reinforcing fiber aligned in the loading direction to yield a highly anisotropic material. Metal-metal, metal-ceramic, metal-plastic, and ceramic-plastic composite materials have been manufactured in an attempt to combine the desirable characteristics of the two component phases.

High temperature applications and space age demands have placed stringent requirements on future materials. A class of composites which possess desirable properties at elevated temperatures are the unidirectionally solidified eutectic alloys (1-4). These composite systems show great potential in aerospace applications because they possess a high strength to weight ratio and morphological stability at temperatures approaching their melting points. The alignment of a whisker-like, intermetallic phase within a ductile matrix provides the anisotropic strengthening while the ductile matrix improves fracture toughness behavior. The thermal stability of unidirectionally controlled eutectic systems is associated with the minimum energy interfaces which result from low-index planes of approximately equal density aligning parallel to the eutectic interfaces (5).

Although binary eutectic composites displayed great promise during early investigations, these alloys lacked the flexibility required in high temperature applications. For example, since the eutectic point is fixed, the volume fraction, the composition, and even the morphology of the phases are invariant within each binary system. In fact, most binary eutectic composites have been eliminated from high temperature applications because they lack high temperature oxidation, sulfidation and thermal shock resistance. For future engineering applications, many investigators have conducted unidirectional solidification studies of multicomponent systems to improve high temperature strength, ductility, oxidation, sulfidation, and thermal shock resistance of controlled eutectic composites. For instance, the $Ni_3Al$-$Ni_3Nb$ eutectic shows great potential as a high temperature structural composite material in a gas turbine environment. This alloy possesses excellent fatigue and impact resistance, strengths up to 140,000 psi at 2000°F, and a density of .3 $lb/in^3$ which is only slightly above that of Ni-base superalloys (6). Furthermore, Lemkey and Thompson have unidirectionally solidified a monovariant eutectic alloy consisting of a cobalt matrix and a carbide reinforcing phase in various shaped crucibles indicating that aligned structure can be produced in complex designs such as turbine blades (7).

The Ni-$Ni_3Nb$ system was selected for the current investigation for two primary reasons. First, this composite has been thoroughly investigated, and it has exhibited attractive mechanical properties: a tensile strength of approximately 110 ksi, and a uniform tensile

elongation greater than 11 percent which far exceeds the ductility of most metal-matrix composites (9-12,14,15,17). Second, the binary Ni-$Ni_3Nb$ composite serves as a prototype model for similar but more complex Ni, Nb, Al, Cr multicomponent systems now being examined for future engineering applications (8).

## 1.2 The Ni-$Ni_3Nb$ Eutectic System - A Review

### 1.2.1 Morphology

Previous investigations have been conducted on the Ni-$Ni_3Nb$ eutectic composite at Lehigh by Quinn (9,10), Hoover (11, 12,13) and Gangloff (14) and in France by Annarumma, et al. (15,16) and Grossiord, et al. (17,18). Unidirectional solidification of this system produces a lamellar eutectic consisting of a fcc nickel-niobium solid solution matrix ($\gamma$) reinforced by 32 volume percent of an ordered orthorhombic ($D_{2h}^{13}$) $Ni_3Nb$ intermetallic phase ($\delta$) (9,10,16). Various investigators (11,12,14,19) have reported the following lattice parameters for the $Ni_3Nb$ phase: $a = 5.07_9\mathring{A}$, $b = 4.57_3\mathring{A}$ and $c = 4.23_0\mathring{A}$. Comparable values were found in other studies (15,16,17).

Quinn (9,10) employed X-ray diffraction methods and found the growth relationship of the eutectic composite to be:

Interface plane || (111) $\alpha$ Ni || (010) $Ni_3Nb$

Growth direction || $[1\bar{1}0]$ $\alpha$ Ni || [100] $Ni_3Nb$.

The same relationship was determined with electron diffraction techniques by Sennicourt and Annarumma (16). Annarumma and Turpin (15) have reported that the aligned $\gamma/\delta$ interface is semicoherent with a lattice mismatch in the close-packed plane $(111)_\gamma$ between .5 percent

along $[1\bar{1}0]_\gamma$ and 3 percent along $[11\bar{2}]_\gamma$. A network of dislocations on $(111)_\gamma$ planes accommodate the lattice mismatch in the $\gamma$ phase.

### 1.2.2 Mechanical Properties and Deformation Mechanisms

Quinn (9,10) reported tensile strengths of 110-125 ksi parallel to the growth direction of the controlled Ni-$Ni_3Nb$ composite which were superior to tensile strengths of the "as-cast" eutectic alloy. Unfortunately, the ultimate strain for all tensile specimens was less than 5 percent. Hoover's subsequent investigation (11,12) of the Ni-$Ni_3Nb$ composite revealed a tensile strength of 105-115 ksi, but with a tensile elongation of 11-15 percent. The composite yielding behavior was characterized by a large elongation under a constant stress with no necking observed prior to fracture. Gangloff (14) reported room temperature tensile strength of 106-110 ksi and an ultimate strain of 14-17 percent. Tensile properties resulting from investigations in France (15,17) are in good agreement with those reported by Hoover and Gangloff. The low ductility of the Ni-$Ni_3Nb$ composite as reported by Quinn, can be attributed to three factors: microstructural misalignment with respect to the growth direction due to non-symmetrical heat flow during horizontal solidification; entrapped non-metallic inclusions within the ingot; and numerous perturbations that existed throughout the entire gauge length resulting from a breakdown of the planar liquid/solid interface during unidirectional solidification.

Quinn (9,10) and Hoover (11,12) used a single surface trace analysis to identify the deformation twins found in the $\delta$ phase, and reported $\{112\}_\delta$ type twinning and subsequent twin boundary crack-

ing which contributed to the overall ductility of the material. The symmetry of all four variants of the $\{112\}_\delta$ plane about the growth axis caused twinning on all twin variants at a constant stress level. Specifically, Hoover found that all the strain in the $\delta$ up to 4 percent was due to $\{112\}_\delta$ twinning while strains in excess of 4 percent resulted from both twinning and subsequent twin boundary fracture. Failure then occurred when a sufficient number of twin boundary cracks accumulated in a given cross-section.

Grossiord's work (17,18) agreed with Quinn's and Hoover's proposed deformation and fracture mechanisms. However, Grossiord employed electron diffraction techniques and found that the twins in the $\delta$ phase were actually {211} type rather than {112} twins as reported by Quinn and Hoover. Gangloff (14) confirmed with a modified two-surface analysis that the twins were, in fact, of the {211} type.

Further transmission electron microscope studies (17) revealed that slip occurred initially on (010) planes in the twinned regions. At greater strains, the untwinned regions were reported to rotate causing the (010) slip plane in the untwinned $\delta$ whisker to be activated. {111} type dislocations were found in the $\gamma$ matrix adjacent to the two-phase interface to accommodate the large stresses caused by twinning of the intermetallic phase. Away from the interface, only a limited amount of slip occurred in the $\gamma$ lamellae.

## 1.3 Fatigue Behavior of Eutectic Composites - A Review

### 1.3.1 Binary Eutectic Systems

Fatigue studies have been conducted on the Al-$Al_3Ni$,

(20,21,22), Al-$CuAl_2$ (20), Ni-Cr (23), Fe-$Fe_2B$ (24), $Ni_3Al$-$Ni_3Nb$ (25), and Ni(Cr)-TaC (26) eutectic alloys in an attempt to generate engineering fatigue data and to better understand crack growth mechanisms in composite materials.

Hoover and Hertzberg (21) investigated the Al-$Al_3Ni$ system and reported a fracture mechanism transition between low stress and high stress fatigue conditions. Under high stress conditions, the $Al_3Ni$ whiskers ruptured in advance of the crack tip. Since the stress concentration under low stress levels was insufficient to cause the fibers to fracture ahead of the crack tip, the fatigue resistance of the matrix was enhanced as the fibers restricted crack propagation. Under this condition, the crack grew through the matrix by Stage I fatigue crack propagation. Ovens and McEvily (22) studied the fatigue behavior of the same composite and similarly reported that the fatigue process was mainly confined to the matrix with the intermetallic fibers restricting the crack propagation. They also stated that grain boundaries, composed of a discontinuous array of whiskers, acted as sources of weakness during fatigue testing.

An investigation (24) of the Fe-$Fe_2B$ eutectic revealed that at room temperature, a sharp fatigue crack resulted in hardening of the matrix at the crack tip which caused a stress concentration sufficient to fracture the brittle fibers in advance of the crack tip. At 500°C, the fatigue crack became very blunt causing smaller stresses to build up ahead of the crack tip. Also, the whiskers were reasonably ductile and not susceptible to brittle fracture at this tempera-

ture. Fatigue crack propagation at 500°C was hindered by the presence of boride fibers, thereby increasing the fatigue resistance of the composite.

Thompson, et al. (25) found that the fatigue resistance of the aligned $Ni_3Al$-$Ni_3Nb$ eutectic was superior to that of a Ni-base superalloy at 1600°F even though the oxidation resistance of the eutectic was inferior to the superalloy. Oxidation played an important role in the fatigue crack propagation at elevated temperatures; for example, during fatigue testing, surface upheavals of oxide produced notches which extended into the interior, and led to specimen failure when the notch reached a critical size.

Low cycle fatigue characteristics of the unidirectionally solidified Ni(Cr)-TaC eutectic composite were studied (26) at room temperature and at 1000°C. Strain cycled tests revealed that the aligned eutectic possessed excellent fatigue resistance even at strain levels which could cause a significant number of fibers to fail in the first cycle. Striations observed on the matrix fracture surface suggested that the fibers failed ahead of the crack front with subsequent crack propagation into the matrix in order to link together the voids formed by the ruptured fibers.

### 1.3.2 The $Ni$-$Ni_3Nb$ System

Hoover (11,13) used notched round bar tensile specimens in tension-tension fatigue studies and found that the $Ni$-$Ni_3Nb$ composite exhibited cyclic lives at stresses above the smooth bar tensile strength. This is not expected in a typical "brittle" composite; however, extensive tensile elongation in this system suggests the possi-

bility that notch strengthening due to plastic constraint may have been responsible for the superior fatigue response of the alloy. In fact, the notched bar tensile strength was 25 percent greater than the smooth bar tensile strength, which supports the notch strengthening hypothesis.

Metallographic examination of the fatigue fracture surfaces revealed that twinning in the δ lamellae was limited to the region directly adjacent to the fracture surface at low stress levels. This reflects the fact that a less severe stress field at the crack tip restricted damage to the area in the immediate vicinity of the fatigue fracture. As the stress environment became more severe, twinning was observed in the δ phase away from the fracture surface, while the γ matrix exhibited evidence of necking.

In low cycle fatigue specimens, striations, oriented parallel to the γ/δ interface, appeared on the γ phase fracture surface suggesting that δ platelets fractured ahead of the crack front. Hoover concluded that the fatigue fracture mechanism at high stress levels was controlled by δ twinning and subsequent twin boundary cracking. Under intermediate stress conditions, the δ platelets did not fracture ahead of the crack front. Rather, the ruptured δ lamellae "...led the crack front..." and contributed to the formation of fatigue striations in the γ matrix which asymptotically approached the γ/δ interface. On low stress-high cycle fatigue fracture surfaces, the Ni-rich lamellae exhibited evidence of faceting, indicative of Stage I crack propagation. As the crack front reached the γ/δ interface, the δ platelet fractured as a result of twin boundary

cracking thereby allowing the crack to continue into the next γ lamellae. Therefore, at low stress levels, fatigue crack propagation was considered to be controlled by Stage I fracture of the γ matrix.

## 1.4 Objective of the Current Investigation

A complete understanding of the mechanical properties of composite materials requires a knowledge of their fatigue response. Although the monotonic behavior of unidirectionally solidified eutectic composites has been thoroughly investigated and understood, their cyclic response has not been fully characterized due to the lack of extensive fatigue studies. Furthermore, no investigation has reported the application of fracture mechanics concepts to fatigue crack propagation data for aligned eutectics. Therefore, the overall objective of the current study is to characterize the cyclic response of the controlled Ni-$Ni_3Nb$ eutectic composite. The fatigue behavior of samples with a controlled microstructure will be compared to the behavior of samples with a non-controlled morphology. For a more complete understanding of crack growth in eutectics, the effect of varying the mean stress, the testing environment, and the thermal history on the fatigue behavior of the composite will be established. Since most fatigue studies of composite materials to date have produced only engineering cyclic data, little effort has been made to describe fatigue crack growth mechanisms. The current study of the cyclic response in the Ni-$Ni_3Nb$ eutectic composite will include an investigation of the crack propagation mechanism. Specific objectives undertaken in this investigation can be outlined as follows:

1. To characterize fatigue crack propagation in the Ni-$Ni_3Nb$ composite in terms of fracture mechanics concepts.
2. To compare the cyclic response of the controlled eutectic in air with the cyclic behavior in a water environment.
3. To define a possible heat treatment that would strengthen the Ni-$Ni_3Nb$ composite by $\delta$ phase precipitation within the $\gamma$ matrix.
4. To determine what effect solidification and heat treatment parameters have on the fatigue crack propagation behavior of the Ni-$Ni_3Nb$ eutectic.
5. To elaborate on the fatigue fracture mechanisms reported by Hoover, and to define a growth rate range where the fatigue fracture mechanism transition occurs.

# CHAPTER II

## THE AGE HARDENING BEHAVIOR OF THE CONTROLLED Ni-$Ni_3Nb$ COMPOSITE

### 2.1 Introduction

The Ni-Nb phase diagram, shown in Figure 1, indicates a significant decrease in the solubility of Nb in Ni between the eutectic temperature, 1282°C, and 1000°C, such that an alloy of eutectic composition should contain 24 volume percent δ phase just below the eutectic temperature, while at 1000°C, 65 volume percent δ should be present. However, previous investigations (9,10,15) have determined that only 30 volume percent δ phase exists at 25°C. The semi-coherent interface made up of a dislocation network apparently hinders diffusion controlled growth of the δ lamellae, thereby, not allowing the supersaturation of Nb atoms in the γ matrix to be relaxed by lamellar thickening. Also, an additional mechanism for the elimination of Nb supersaturation in the γ phase through δ precipitation is not active to any great extent (9-12,14). However, Annarumma and Turpin (15) reported low density Widmanstatten precipitation on all four variants of the $\{111\}_\gamma$ plane along with a fine equiaxed δ precipitate.

During the current investigation, cellular precipitation of the δ phase was observed in large proeutectic γ dendrites, indicating that Nb supersaturation in large γ regions can be relieved through precipitation. A typical proeutectic γ dendrite containing the cellular precipitate is shown in Figure 2a. In properly aligned, lamellar structure, however, no δ precipitation in the γ lamellae was observed.

Gangloff (14) reported some δ phase Widmanstatten precipitation

in tensile specimens tested at 830°C to 1000°C. The distribution of precipitation was uneven as some lamellae were filled with δ precipitates while others contained none. It was observed that as the testing temperature increased the density of precipitation increased. Gangloff employed a single surface trace analysis to confirm Annaruma's observation (15) that the precipitate formed on the $(111)_\gamma$ habit plane. δ phase Widmanstatten precipitation was also found in 750°C creep rupture specimens deformed for periods of time in excess of 4.1 hours. Again, the overall distribution of the precipitate was non-uniform, and the density of the precipitation increased as the time at 750°C increased. Forero (27), while studying diffusion bonding of the Ni-$Ni_3Nb$ composite, reported a non-uniform distribution of δ precipitates in the γ matrix in samples bonded at 820° under a pressure of 56.9 ksi with a 6 hour dwell time. Under comparable bonding conditions, Hill (28) also observed a low-density of δ phase Widmanstatten precipitation.

To investigate the possible effect of δ precipitation on the mechanical behavior of the Ni-$Ni_3Nb$ composite, Gangloff (14) aged the controlled structure at 1000°C for periods of time up to 100 hours which resulted in a non-uniform, low density precipitation of δ. These thermal treatments resulted in an increase in hardness of 2 $R_C$ points, independent of the aging times studied. Since the density of the δ precipitate in heat treated specimens was much less than the density observed in hot tensile testing, Gangloff concluded that the precipitation of the δ phase in the γ matrix was stress assisted.

Since precipitation hardening of the γ lamellae in the Ni-$Ni_3Nb$ system was still considered possible and of significance in the development of more sophisticated eutectic alloy systems, further heat treat studies were indicated. Specifically, it was felt that an initial solution treatment of this alloy would increase the Nb supersaturation in the nickel lamellae, thereby enhancing the chances for eventual precipitation during subsequent aging.

## 2.2 Presentation and Discussion of Results

### 2.2.1 Microstructure

The Ni-$Ni_3Nb$ interlamellar spacing (λ) was found to conform to the equation

$$\lambda^2 R = \text{constant} \qquad (1)$$

where λ = interlamellar spacing

R = solidification rate

Typical lamellar spacing for solidification rates (R) of .8 cm/hr, 2 cm/hr and 4.7 cm/hr was 14 μ-16 μ, 8 μ-11 μ, and 6 μ-9 μ, respectively. As expected, the as-controlled microstructure obtained during the current investigation was free of δ phase precipitation as shown in Figure 2b.

When the as-grown composite was aged for 3 hours and 10 hours at 1000°C, very few δ precipitates were formed in agreement with Gangloff's findings (14). In fact, Widmanstatten δ precipitates were observed only in the thick γ lamellae as illustrated in Figure 3a. The amount of δ precipitation increased slightly in the sample aged for 10 hours.

On the other hand, solution treating and aging (see Appendix I: Heat Treatment) of unidirectionally solidified Ni-$Ni_3Nb$ composites grown at .8 cm/hr, 2 cm/hr and 4.7 cm/hr produced a uniform distribution of δ precipitation of Widmanstatten morphology within the γ matrix as shown in Figure 3b. Single surface trace analysis revealed that the precipitate formed on all four variants of the $\{111\}_\gamma$ habit plane, consistent with Gangloff's (14) and Annarumma's (15) findings. As expected, no precipitation of the γ phase was observed within the intermetallic lamellae.

The data obtained from quantitative metallography (see Appendix I: Quantitative Metallography) of the Ni-$Ni_3Nb$ composite with various thermal histories appears in Table I. The as-controlled structure consisted of 31.8 ± 1.6 volume percent δ phase in good agreement with Quinn's (9,10) and Annarumma's (15) observations. However, this value is far below the equilibrium amount of δ phase that should exist at room temperature. After solution treating, within 60°C of the eutectic temperature, the total amount of δ phase dropped to 27.0 ± 1.3 volume percent while no δ precipitation was observed. This drop was expected since the phase diagram suggests that just below the eutectic temperature 24 volume percent should exist. The lower amount of δ phase present indicates that the γ phase possesses a much richer supersaturation of Nb atoms, thereby enhancing the driving force for precipitation to occur during subsequent aging. In fact, precipitation of the δ phase was observed in the solution treated samples after they were aged at 1000°C for 1 hour. Measure-

ments of the solution treated and aged composite microstructure revealed that the volume fraction of the δ lamellae increased to 33.2 ± 1.1 percent, approximately equal to the amount of δ phase present in the as-grown structure. The δ phase Widmanstatten precipitates within the γ matrix accounted for an additional 9 volume percent, making the total amount of δ phase present approximately 42 volume percent. As noted in Table I, similar results were obtained in the sample solution treated and aged for 100 hours. The total amount of δ phase present after age hardening is closer to the amount predicted by the equilibrium phase diagram, but still over 20 volume percent less than the equilibrium amount, thereby indicating that metastable equilibrium still persists. These results suggest that the lack of diffusion across the semi-coherent interface hinders lamellar thickening, and the sluggish nature of the Widmanstatten precipitation prevents the complete relaxation of the Nb atoms in the γ phase.

### 2.2.2 Micro-Hardness Results

Micro-hardness results obtained from the Ni-$Ni_3Nb$ composite with various thermal histories appear in Table II. The as-controlled hardness of 323.7 ± 3.8 DPH corresponds to a hardness value greater than that reported by Gangloff (14), 27-29 $R_c$. However, Gangloff used a lower initial Nb content, 22.3 weight percent, approximately .7 weight percent less than the amount used during the current investigation, and quantitative metallography of his as-grown ingots revealed that only 29.3 ± 1.4 volume percent δ was present in his eutectic structure. These factors could account for the discrepancy in the hardness values reported by Gangloff, and those found during

this investigation.

Solution treating of the aligned composite caused the hardness to drop from 323.7 $\pm$ 3.8 DPH to 312.7 $\pm$ 6.1 DPH. Rhodes, et al. (28) observed the opposite effect in the Al-$CuAl_2$ eutectic system since the increase in Cu content within the matrix, as a result of the solution treatment, strengthened the composite. In the Ni-Ni$_3$Nb system, the Nb content in solid solution in the $\gamma$ matrix increased as a result of solution treating thereby contributing toward an enhanced solid solution hardening effect; apparently, this effect was more than counterbalanced by the decrease in the amount of $\delta$ phase reinforcement from 32 to 27 volume percent.

The sample that was solution treated and aged for 1 hour and the as-controlled sample contained approximately the same volume fraction of $\delta$ lamellae, while the thermally treated specimen contained an additional 9 volume percent $\delta$ phase in the form of Widmanstatten precipitation in the $\gamma$ matrix. It is felt that this additional $\delta$ precipitate can strengthen the ductile matrix and thereby strengthen the composite. To wit, the hardness of the age hardened sample was found to be 341.4 $\pm$ 3.8 DPH, and, therefore, greater than both the as-grown and as-quenched hardnesses. The specimen solution treated and aged for 100 hours yielded approximately the same hardness value, 342.3 $\pm$ 7.4 DPH. This result was expected since the total amount of $\delta$ phase present in the age hardened sample was not found to be dependent on the aging time.

# CHAPTER III

## FATIGUE CRACK PROPAGATION IN THE Ni-$Ni_3Nb$ COMPOSITE: A FRACTURE MECHANICS APPROACH

### 3.1 Introduction

Fracture mechanics concepts have been successfully applied to crack growth during cyclic loading. The stress intensity factor range, $\Delta K$ (i.e., $K_{max}-K_{min}$), was found to correlate well with fatique crack propagation (FCP) in fcc, bcc and hcp metals as shown by Paris (30,31).

$$\frac{da}{dN} = C\,\Delta K^{n} \qquad (1)$$

where $\Delta K = Y\,(\frac{a}{W})\,\Delta\sigma\,\sqrt{\pi a}$

$\sigma$ = gross stress

a = crack length

W = panel width

Y = geometrical correction factor

C,n = material constants

The proportionality constant, C, has been shown to depend on the relative mean load and the material. A value of n equal to 4 has been found for a variety of metals (30,32). Maria Ronay (32) using an energy approach has shown that the value of n for any metal is bounded by 2 for the case of maximum ductility, and by 6 for the case of perfect elasticity.

Hoover (11,13) found that the Ni-$Ni_3Nb$ composite illustrated several interesting fatigue properties. The ability of the composite

to notch strengthen resulted in cyclic lives at stresses above the smooth bar tensile strength. Also, the aligned eutectic exhibited a notched bar endurance limit of 55 percent of the smooth bar tensile strength which is considered outstanding for nickel based alloys.

The objective of this study was to employ a fracture mechanics approach in order to characterize the FCP behavior in Ni-$Ni_3Nb$ alloys under various metallurgical conditions and environments.

## 3.2 Fatigue Testing

### 3.2.1 Test Sample

A number of different testing configurations can be employed to obtain FCP data. However, due to the size of the unidirectionally solidified ingot, approximately 9/16" diam. x 6", conventional fatigue specimens could not be used. Consequently, a four-point bending configuration was used in the fatigue test program. Test specimens, 1/2" x 1/10" x 4 1/2" as shown in Figure 4, were electro-discharge machined from cylindrical as-grown ingots. A starting notch, approximately .05" deep, was introduced normal to the long dimension in the middle of the slab. Note that four steel tabs were epoxy bonded to the extremities of the specimen to prevent buckling and damage to the sample during cycling.

### 3.2.2 Four-Point Bending Fatigue Apparatus

Loads were applied to the fatigue sample through the four-1/4" diameter loading pins with the major span equal to 4" and the minor span equal to 3" (Figure 5). The crack tip was subjected to tension-tension loading, and the fatigue crack propagated vertically.

Cyclic tests were performed on an MTS electrohydraulic closed loop testing machine with a cyclic frequency of 10 and 20 Hz. Cycling was interrupted periodically in order to measure the increment of crack extension (about .005 inch), and to record the associated number of cycles.

### 3.2.3 Test Specimen and Loading Fixture Design Verification

Before fatigue tests were conducted on the eutectic composite, it was first necessary to prove that good data could be obtained from the previously described loading fixture. T-1 steel was chosen for this test since its mechanical properties were similar to those of the Ni-$Ni_3Nb$ composite and the FCP of T-1 steel had been thoroughly investigated at Lehigh (33,34). Samples of T-1 steel were prepared to the same dimensions as described in Section 3.2.1. The FCP response of the conventional steel alloy when tested in the four-point bending fixture, was slightly greater than the crack growth rates previously observed (data band) by Parry (Figure 6). Note that at higher levels, the discrepancy increased.

The discrepancy between the data obtained in the present test and the previous conventional tests can be accounted for by applying plasticity corrections to the crack propagation data. Ahead of the advancing crack tip, a plastic zone as illustrated in Figure 7, exists, and as an approximation, the effective crack length may be set equal to the actual crack length plus the plastic zone size, $r_y$:

$$a_{eff} = a_{actual} + r_y \tag{2}$$

where

$$r_y = \frac{1}{2\pi} \frac{K^2}{\sigma_{Y.S.}^2} \tag{3}$$

Since the geometrical correction factor, Y, is a function of a/W, an additional plastic zone correction is necessary, especially since Y is so sensitive to crack length in small sample used in this investigation (Figure 8). Thus, an effective stress intensity factor range, given by the following equation:

$$\Delta K_{eff} = Y \left[\frac{a_{eff}}{W}\right] \Delta\sigma \sqrt{\pi(a_{eff})} \qquad (4)$$

was determined by an iterative process since the plastic zone size is dependent on the stress intensity level. When the plasticity corrections are introduced to the data shown in Figure 6, results are seen to be in much better agreement, Figure 9. It is important to note that in conventional testing, the plastic zone size is usually much smaller than the total crack length and is often ignored in computations of $\Delta K$. However, with the specimen and testing fixture design employed during the current investigation, it was necessary to make the adjustment for plasticity at the crack tip since the ratio of plastic zone size to the crack length is significantly larger, and the value of Y increases very rapidly in four-point bending. Having established that accurate fatigue data could be obtained using this specimen configuration in four-point bending when plastic zone size corrections are applied, samples of the Ni-$Ni_3Nb$ composite were tested.

## 3.3 Presentation and Discussion of Results

### 3.3.1 FCP in the Unidirectional Solidified Ni-$Ni_3Nb$ Composite

The data shown in Figure 10 which characterize the FCP

response of the aligned eutectic at a load ratio ($R = \frac{\text{minimum load}}{\text{maximum load}}$) of less than .1, represent the first such reported information for eutectic composites. Note that an excellent correlation exists between the stress intensity factor range and the fatigue crack growth rates in this in situ composite. From Equation 1, the experimental constants are found to be

$$C = 4 \times 10^{-13} \quad (\Delta K: \text{ksi}\sqrt{\text{in}} \text{ units})$$

$$n = 4.9$$

for growth rates between $10^{-7}$ in/cyc and $10^{-4}$ in/cyc. The value of "n" for the composite was slightly higher than that found in most conventional alloys, 4.9 versus 4.0, but this value was well below the theoretical upper limit of 6 derived by Ronay (32). The FCP response of the Ni-$Ni_3Nb$ composite was similar to that of steel alloys with comparable elastic moduli. This result was expected since Pearson (36) has illustrated that the crack growth rates of various metals may be normalized by plotting da/dN vs $\Delta K/E$ where E is the modulus of elasticity.

### 3.3.2 Effect of Test Variables on FCP

The results of additional fatigue testing conducted at a load ratio of 0.5 were compared with the previous results (data band) as seen in Figure 11. As expected (31) a small shift in crack growth rates resulted from the elevated mean stress intensity. It is important to note that $\Delta K$ rather than $K_{mean}$ was the most important factor controlling crack propagation since an increase in $K_{mean}$ by a factor of two only caused da/dN to triple, while doubling the value of $\Delta K$ caused a 30 fold increase in da/dN.

The crack growth behavior of the controlled Ni-$Ni_3Nb$ composite tested in a water atmosphere was compared with the FCP response of the aligned eutectic tested in an air environment (data band) as shown in Figure 12. The presence of water at the crack tip had no significant effect on the growth rates as all data points were very close to the upper boundary of the data band.

3.3.3 Effect of Metallurgical Variables on FCP

Metallurgical variables such as crystallographic texture and thermo-mechanical processing usually have little effect on the FCP response of conventional alloys (37). However, the fatigue growth rates of the non-aligned eutectic alloy were significantly greater than that of the unidirectionally solidified composite as illustrated by Figure 13. Furthermore, the as-cast alloy underwent static fracture at a much lower stress intensity factor than did the as-controlled eutectic, indicating that the non-aligned structure possessed much lower toughness. Therefore, the properly aligned eutectic alloy is found to possess superior fatigue and fracture toughness behavior than does the non-controlled alloy. This was believed due to large and randomly oriented particles of $\delta$ which presumably failed prematurely.

Thermal treatment of the unidirectionally solidified Ni-$Ni_3Nb$ eutectic composite caused an unexpected change in the fatigue response of the alloy. Fatigue tests conducted on the age hardened composite (thermal treatment outlined in Appendix I: Heat Treatment) revealed a significant decrease in the crack propagation rates when compared to the fatigue behavior of the as-grown alloy (data band) as

shown in Figure 14. The presence of δ phase Widmanstatten precipitation in the γ matrix appears to have retarded crack growth in the γ' phase thereby improving the fatigue behavior of the composite. This effect has important implications since the age hardening of the aligned structure can lead to an improvement in strength, as inferred from the hardness measurements, and an enhancement of fatigue performance.

# CHAPTER IV

## FATIGUE FRACTURE SURFACE APPEARANCE

### 4.1 Introduction

Electron fractographic techniques have revealed that certain microscopic features on fracture surfaces can be correlated to specific modes of failure. Numerous investigators (38-42) reported that the general appearance of the fatigue fracture surface could provide important information in post fracture analysis. FCP in face-center-cubic metals and alloys propagate in various modes; for instance, under low stress conditions, fatigue cracking can initiate and propagate in a crystallographic shear mode, designated Stage I, producing planar facets. Electron fractographic examination of Stage I fracture surfaces often reveals almost featureless facets which suggests that the two fracture surfaces had rubbed together during crack propagation. Stage I crack growth usually occurs on a fracture plane approximately 45° to the tensile axis. Forsyth, et al. (38,39) found that fatigue cracks initially grew by an "unslipping or reverse glide mechanism" which created a surface crevice or intrusion that deepened with time. This reverse glide mechanism was termed Stage I FCP, and was characterized by crystallographic fracture facets. Forsyth postulated that reverse slip decreased the cohesive strength across the slip plane resulting in further crack extension. Cracks formed on planes of approximately maximum shear stress giving the fracture surface a crystallographically faceted texture. McEvily and Boettner (43) also described Stage I FCP as an extension of the crack initiation process which involved cyclic shear

and cross-slip of screw dislocations. Laird (44,45) has extended the plastic blunting process of crack propagation to describe Stage I FCP, where plastic deformation along the crack front resulted in the blunting and extension of the crack tip.

Gell and Leverant (46-48) conducted high cycle fatigue tests on the nickel-base superalloy, Mar-M200, and observed Stage I facets on {111} type planes that contained distinctive features--rather than the featureless facets usually reported during the shear mode crack propagation--which were not decimated by rubbing. The presence of distinct markings reported on the fracture surface suggested that normal stresses as well as shear stresses were involved in Stage I crack propagation. As a result, Gell and Leverant (47) proposed a model describing Stage I FCP as reversed slip on a small number of slip planes in advance of the crack front which weakened the cohesive strength of the atomic bonds in a very small area--similar to Forsyth's (38,39) hypothesis. In addition, Gell and Leverant believed that sufficient weakening of the atomic bonds allowed low tensile stresses to initiate local cleavage which resulted in the crystallographic appearance even though the crack front propagated in a cyclic manner. Under low-cycle fatigue conditions, the size of slip bands and the strain within the bands increased causing greater plastic deformation at the crack tip. Gell and Leverant concluded that the resolved shear stress controlled the size of the weakened band, and that crack growth rates were dependent on the maximum normal stress.

Stage II FCP, the tensile mode of crack growth, usually occurs on a fracture plane normal to the tensile axis. Striations, associ-

ated with each successive position of the advancing crack front, have been observed on the fracture surfaces of many metals (38,49,52). Numerous models based on crystallographic (40,41,50) and noncrystallographic (42,46,52) considerations have been proposed to explain the formation of striations on the fracture surface. Previous investigators (40,42,53) found an excellent correlation between the stress intensity factor range and the measured striation spacings over a range from $10^{-6}$ to $10^{-4}$ inches per striation spacing in aluminum, steel and titanium alloys. Furthermore, good agreement was reported between the striation spacing and the macroscopic crack growth rates in the range of $10^{-5}$ in/cyc (40,42).

Numerous investigators have reported the presence of striations during Stage I crack growth. Stubbington and Forsyth (39) suggested that the deformation markings observed on the Stage I fracture surface of high strength aluminum alloys may have been the result of a tensile mode FCP. Ham and Wayman (53), who studied the FCP in T.D. Nickel, observed both Stage I FCP and striations normal to the crack growth direction in the same regions. Gell and Leverant (43) reported striations on the Stage I fracture surface in the Ni-base alloy Mar-M200.

In a previous investigation of the fatigue fracture mechanisms operating in the unidirectionally solidified Ni-$Ni_3Nb$ eutectic composite, Hoover (11,13) reported that a fracture mechanism transition occurred between high cycle and low cycle fatigue conditions. Under high stress-low cycle fatigue conditions, $\delta$ lamellae fractured ahead of the advancing crack tip by twin boundary cracking, thereby creating long voids adjacent to the $\gamma$ lamellae. Crack propagation into the

unbroken γ lamellae occurred by "...cyclically induced void growth and coalescence...," and produced fatigue striations, characteristic of Stage II FCP, parallel to the γ/δ interface. Hoover concluded that under this condition, fatigue resistance was controlled by the fracture of the δ platelets. Low stress-high cycle fatigue resistance was found to be controlled by the Stage I crack propagation along active slip planes in the γ lamellae. More specifically, Hoover proposed a fracture mechanism where the fatigue crack propagated through the matrix, and as the crack front reached the reinforcing phase, δ twinning and subsequent twin boundary rupture occurred, thereby allowing the crack to continue into the next γ lamellae. Hoover used information from metallographic sections of fatigue fractures to report that twinning in the δ phase occurred in the regions immediately adjacent to the fracture at low stress levels, while under higher stress conditions twinning was reported farther from the fractured surface.

For a more complete understanding of the fatigue response of eutectic composites, metallographic and fractographic techniques were utilized during the current investigation in order to characterize the mechanisms operating during FCP in the Ni-$Ni_3Nb$ composite as a function of the pervailing stress intensity factor at the crack tip.

## 4.2 Fractographic Observations

### 4.2.1 High FCP Rates: (Greater than $1.5 \times 10^{-5}$ in/cyc)

Under high stress intensity range conditions, Stage II crack propagation occurred by fatigue striation formation in the γ

phase (Figure 15a). Figure 16 illustrates that the microscopic growth rates in the $\gamma$ phase (broken lined boxes) were in good agreement with the macroscopic growth rates (data band) over a range of growth rates from $3 \times 10^{-6}$ to $2 \times 10^{-5}$ in/cyc. Striations always formed parallel to the $\gamma/\delta$ interface independent of the $\delta$ platelet orientation with respect to the crack front as shown in Figure 15b which reveals two $\delta$ platelets surrounded by the striated $\gamma$ matrix. Note that the direction of crack growth was normal to the interphase boundary as evidenced by the fact that striations always remained parallel to the $\gamma/\delta$ interface. Therefore, under high $\Delta K$ conditions, the fatigue fracture mechanism is controlled by the Stage II FCP through the $\gamma$ matrix. Similar scanning electron microscopy findings were in support of the transmission electron microscopy studies.

$\delta$ platelets fractured as a result of $\{211\}_\gamma$ type twinning and subsequent twin boundary cracking at all growth rates. Tongues and steps observed on the $\delta$ phase fracture surface (Figure 17a) were found to be related to the four variants of the $\{211\}_\delta$ type twin. Twin boundary fracture occurred along one variant of the $\{211\}_\delta$ twin while the other three variants intersected the fracture surface. Steps resulted from a change in orientation of the fracture surface due to the intersecting secondary $\{211\}_\delta$ twin while tongues were caused by localized crack plane deviations.

Fins along the $\gamma/\delta$ interface, indicative of decohesion between the mating phases, were observed under both high and low $\Delta K$ conditions. Figure 17b illustrates an example of the fins which exist at the interphase boundary.

### 4.2.2 Low FCP Rates: (Below 5 x $10^{-6}$ in/cyc)

As Hoover (11,13) had reported at low growth rates, the $\gamma$ phase fractured in a faceted manner indicative of Stage I FCP along active slip planes. The stereographic pair seen in Figure 18 and the electron fractographs shown in Figure 19, illustrate the very crisp facets (indicated by the letter F on Figure 18) present at low growth rates. Beachem and Meyn (54,55) have termed this mode of separation where the metal parts along a glide plane as "glide plane decohesion." The observation of Stage I facets on the $\gamma$ matrix fracture surface is consistent with the low stress, high cycle fatigue findings of Gell and Leverant (46-48). Figure 19b also shows evidence of interphase boundary decohesion since fins appeared at the $\gamma/\delta$ interface.

Parallel fracture markings often superimposed on the Stage I facets are shown in Figure 20a. Due to the fine width of the fracture markings, measurements of their spacings were conducted at much higher magnifications (Figure 20b). The spacing of the parallel lines, approximately 600Å, was independent of the applied stress intensity range as shown in Figure 16 (solid boxes) which indicates that parallel fracture markings are definitely not fatigue striations. Furthermore, when the parallel fracture markings and striations appeared in the same region, the spacing of the fracture markings was always two or three times smaller than that of the striations as indicated on Figure 16 where the boxes labelled 1-1*, 2-2* and 3-3* correspond to the spacing of the fine lines and striations, respectively. The parallel markings were always observed parallel to the $\gamma/\delta$ interface, which also corresponds to a trace of the $\{111\}_\gamma$ plane

(the slip plane in fcc metals). This suggests that the fracture markings may be the result of slip offsets formed as a result of the severe stresses present at the crack tip. Gell and Leverant (46) reported a similar series of parallel markings on the fatigue fracture surface of the Ni-base superalloy, Mar-M200, which corresponded to traces of the $\{111\}_\gamma$ plane. Gell and Leverant believed that these parallel markings were slip offsets associated with the relaxation of the stress field at the crack tip after the crack had passed.

Straight slip lines are usually found in materials that exhibit planar slip, favored by a low stacking fault energy. While the stacking fault energy of pure nickel is very high, approximately 250 erg/cm$^2$ (56), the addition of niobium to the nickel causes a significant decrease in the stacking fault energy. In fact, Annarumma and Turpin (15) suggested that the stacking fault energy was "... certainly below 50 erg/cm$^2$ ..." Hill (28) calculated the stacking fault energy of the $\gamma$ phase from a dissociated three-fold node and obtained a value of 14 erg/cm$^2$. These low values for the stacking fault energy are consistent with the very straight slip lines observed in the $\gamma$ phase during the current investigation.

The fact that distinct features on the Stage I fracture surface, such as crisp facets and parallel and parallel fracture markings, were not obliterated by rubbing suggests that local shear and normal stresses controlled the Stage I crack growth in the $\gamma$ phase--consistent with Gell and Leverant's (47) studies.

### 4.2.3 Fracture Mechanism Transition: ($5 \times 10^{-6}$ in/cyc - $1.5 \times 10^{-5}$ in/cyc.)

At intermediate growth rates, a transition from Stage I to Stage II FCP occurred as evidenced by the fact that regions containing both facets (indicated by the letter F) and striations were observed on the $\gamma$ phase fracture surface as shown in Figure 21a. This observation was consistent with previous investigations (39,43, 53). It is of significance to note that $\gamma$ phase facets were poorly defined when compared to the crisp facets observed under low $\Delta K$ conditions suggesting that a noncrystallographic fracture had occurred. The interwoven appearance of the $\gamma$ phase fracture surface, as seen in Figure 21b, is evidence of serpentine glide defined by Beachem and Meyn (52,53) as partial glide plane decohesion on several slip planes. Evidence of poorly defined facets and serpentine glide, suggests that gliding occurred on multiple sets of intersecting planes. Since high $\Delta K$ levels were associated with the intermediate growth rates, more slip systems could operate, thereby increasing the dislocation activity on a number of intersecting slip planes ahead of the crack tip. Such dislocation activity probably weakened the cohesive energy of atomic bonds along a number of intersecting slip planes thereby producing a noncrystallographic or poorly defined faceted appearance. Finally the increased local normal stresses under intermediate $\Delta K$ conditions associated with the fracture mechanism transition, resulted in the formation of striations indicative of a tensile mode fatigue fracture.

## 4.3 Metallographic Observations

Metallographic examination of the fractured specimens has provided important information in determining the fatigue crack growth mechanisms of the Ni-$Ni_3Nb$ eutectic composite. $\{211\}_\delta$ twinning was observed in the regions adjacent to the fracture surface. Figure 22a represents a typical area in the fracture profile which illustrates $\{211\}$ type twinning in the $\delta$ lamellae and subsequent twin boundary carcking. Under low stress intensity factor conditions, less than approximately 30 ksi/in, $\{211\}_\delta$ twinning was observed only in the immediate vicinity of the fatigue fracture, thereby indicating that a less severe stress field existed at the crack tip which confined the deformation damage to the area very near the fatigue crack as Hoover (11,13) had reported. On the other hand, twinning was not restricted to the immediate vicinity of the fracture surface at high $\Delta K$ levels. Under both high and low $\Delta K$ conditions, twin boundary cracking was limited to the region immediately adjacent to the fatigue crack.

In addition to several variants of $\{211\}_\delta$ type twins, an additional twin mode may be seen in Figure 22b which appears to lie approximately parallel to the $\gamma/\delta$ interface in a longitudinal section. A second deformation twinning system in the $Ni_3Nb$ phase was reported and unambiguously identified as a $\{011\}_\delta$ type twin by Hoover (11,12) and Grossiord and Turpin (18). The fact that the second twin mode observed during the current investigation was approximately parallel to the growth direction is consistent with the $\{011\}_\delta$ type twinning reported by Hoover and Grossiord and Turpin. This additional twin

variant was found only at high ΔK levels where the triaxial stresses were greatest in good agreement with Grosskreutz and Turpin's findings that $\{011\}_\delta$ twins could only be activated under high triaxial stress conditions since the shear direction for $\{011\}_\delta$ type twins is nearly parallel to the tensile axis.

At low growth rates, secondary fatigue cracks propagated parallel to the fatigue fracture surface as seen in Figure 23a. (Etchant A was employed in order to distinguish the two phases; however, this etch does not reveal δ phase twins.) Upon closer examination, it is seen (Figure 23b) that a number of reinforcing δ plates had undergone twin boundary fracture ahead of the advancing crack front. (The macroscopic FCP rates in this region were less than $1.4 \times 10^{-6}$ in/cyc well within the region where the γ matrix failed as a result of Stage I FCP.) The fact that δ platelets fractured ahead of the crack tip indicates that the twin boundary fissures subsequently grew into the γ matrix by Stage I FCP. Thus, the Stage I fracture along active slip planes in the γ matrix controls the FCP at low growth rates as well as at high growth rates. This proposed fracture mechanism contradicts the one postulated by Hoover (11,13) who postulated that for the low growth rate regime, δ platelets fractured as the crack front reached the γ/δ interface. However, the current investigation has revealed that the δ whiskers fractured well ahead of the advancing crack tip.

# CHAPTER V

## CONCLUSIONS

Based on the experimental results and the subsequent discussion, the following conclusions have been drawn:

A. Age Hardening Behavior

1. Proper solution treatment and aging of the Ni-$Ni_3Nb$ composite produced a uniform distribution of $\delta$ phase precipitation of Widmanstatten morphology.
2. A condition of metastable equilibrium persists after proper age hardening since the total $\delta$ phase was still twenty percent below the equilibrium amount.
3. Micro-hardness of the composite was found to be dependent on the total amount of $\delta$ phase present.

B. Fatigue Crack Propagation Rates

1. A power relationship between da/dN and $\Delta K$ was found to exist for the aligned Ni-$Ni_3Nb$ composite over a range of growth rates from $10^{-7}$ in/cyc to $10^{-4}$ in/cyc. The FCP behavior of this alloy was analogous to that of steel alloys with comparable elastic moduli.
2. A small shift to higher growth rates was observed as a result of higher mean stress intensity levels, however the stress intensity factor range rather than the mean stress intensity level was the major variable controlling the FCP response.

3. A water environment at the crack tip was found to have no significant effect on FCP.

4. The fatigue behavior and toughness of the non-controlled structure was inferior to that of the aligned composite.

5. The presence of δ phase precipitates of Widmanstatten morphology within the γ matrix as a result of age hardening thermal treatment retarded FCP in the γ phase, thereby improving the fatigue response of the composite.

C. Fatigue Crack Propagation Mechanisms

1. During Stage II FCP in the γ matrix fracture surface, microscopic growth rates--striation spacings--were in good agreement with macroscopic crack growth rates. At low growth rates, the γ fracture surface exhibited facets indicative of Stage I FCP along active slip planes. Under all $\Delta K$ levels, δ lamellae fractured as a result of {211} twinning and subsequent twin boundary cracking ahead of the advancing crack tip.

2. The fatigue behavior of the unidirectional solidified Ni-$Ni_3Nb$ eutectic underwent a fracture mechanism transition at intermediate growth rates ($5 \times 10^{-6}$ in/cyc to $1.5 \times 10^{-5}$ in/cyc) as evidence of both Stage I and Stage II FCP was observed on the fracture surface.

3. The γ matrix appeared to be the major factor controlling the FCP response of the composite.

TABLE I

Data Obtained from Quantitative Metallography of U.D.S. Ni-$Ni_3Nb$ Specimens

| | Volume % δ lamellae | Volume % δ* ppt in γ matrix | Volume %** δ ppt | Total Volume % δ phase |
|---|---|---|---|---|
| As-Controlled | 31.8 ± 1.6 | - | - | 31.8 ± 1.6 |
| Solution Treated and Quenched | 27.0 ± 1.3 | - | - | 27.0 ± 1.3 |
| Solution Treated and Aged 1 hour | 33.2 ± 1.1 | 13 | 9 | 42 |
| Solution Treated and Aged 100 hours | 31.5 ± 1.1 | 13 | 9 | 40 |

* Calculated from an Electron Microscope Replica of the polished sample. (See Appendix 1: Quantitative Metallography.)

** Volume % δ ppt = (Volume % δ ppt in γ matrix) x (1-Volume fraction of δ lamellae).

TABLE II

Data Obtained from Micro-Hardness Testing of U.D.S. Ni-$Ni_3Nb$ Specimens

| | D. P. H. | |
|---|---|---|
| | Range | Mean. |
| As-Controlled | 317 - 328 | 323.7 ± 3.8 |
| Solution Treated and Quenched | 305 - 320 | 312.7 ± 6.1 |
| Solution Treated and Aged 1 hour | 336 - 349 | 341.4 ± 3.8 |
| Solution Treated and Aged 100 hours | 332 - 349 | 342.3 ± 7.4 |

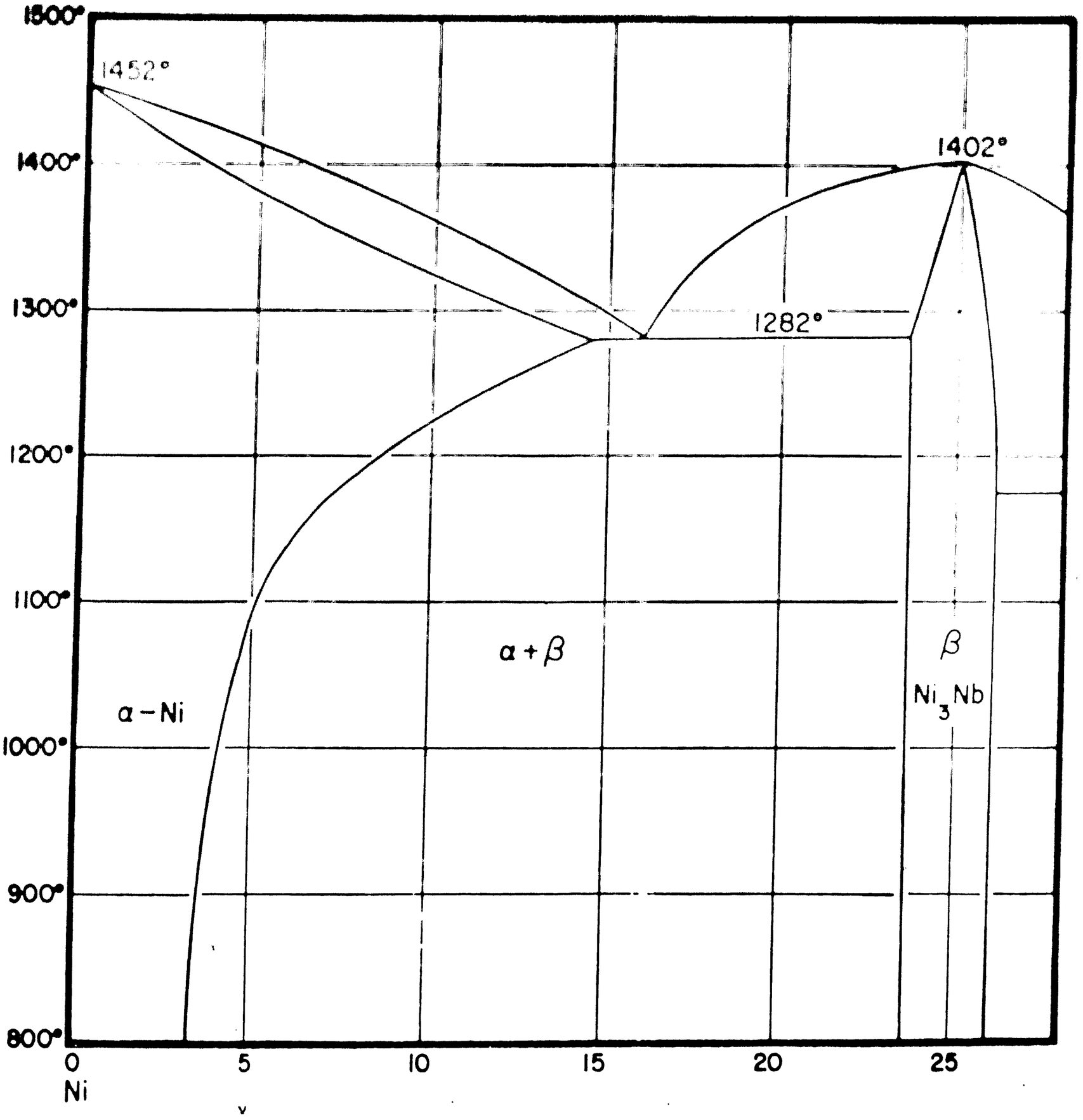


# EQUILIBRIUM PHASE DIAGRAM

Figure 1 - Ni-Nb equilibrium phase diagram; Ni end (19)

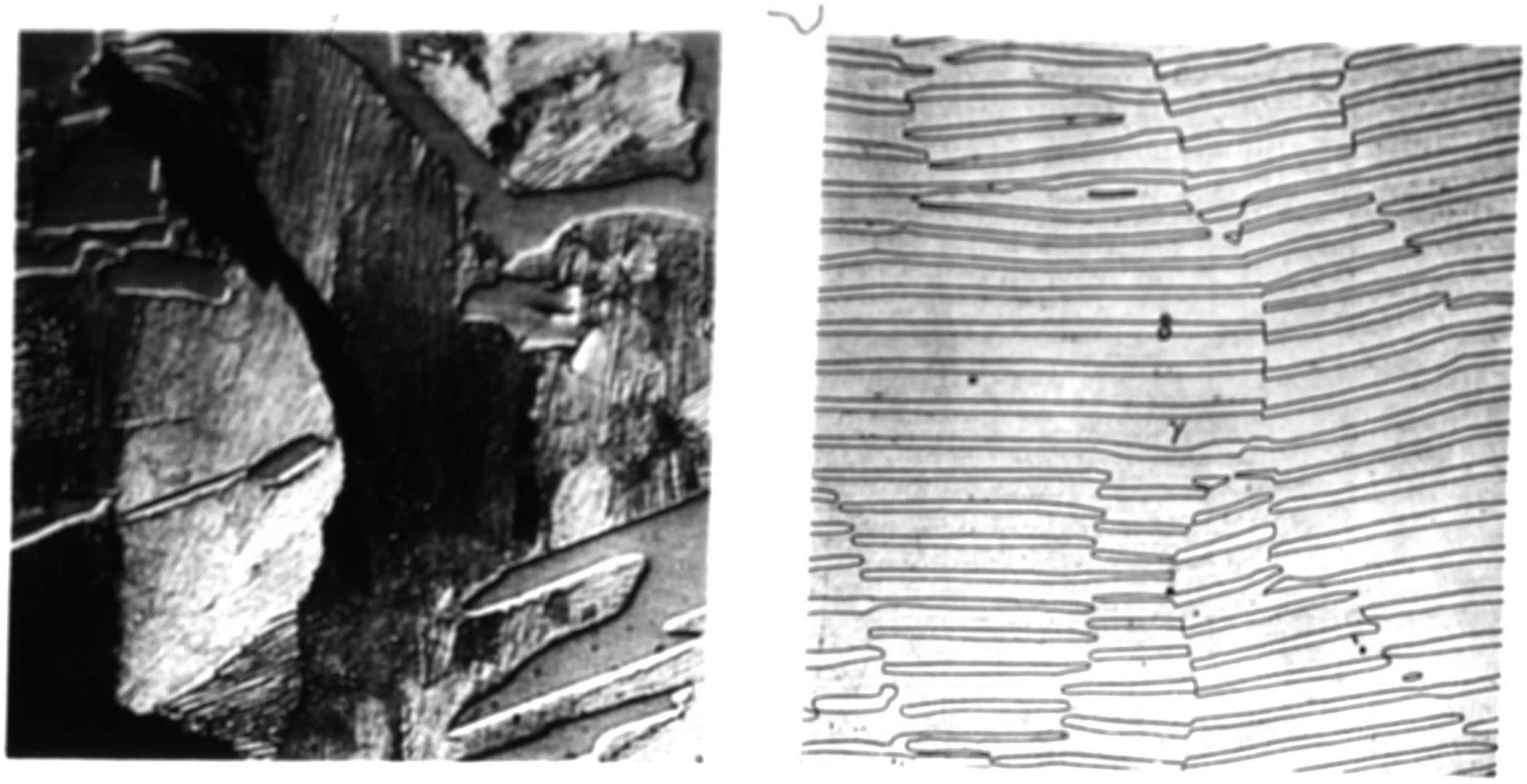


(a) (b)

Figure 2: Photomicrographs of as-grown structure.
(a) Cellular precipitation within a large proeutectic dendrite present in a Ni-rich ingot. 720X. (Interference Microscope)
(b) Aligned lamellar microstructure illustrating the absence of δ phase precipitation in on-composition ingots. 533X.

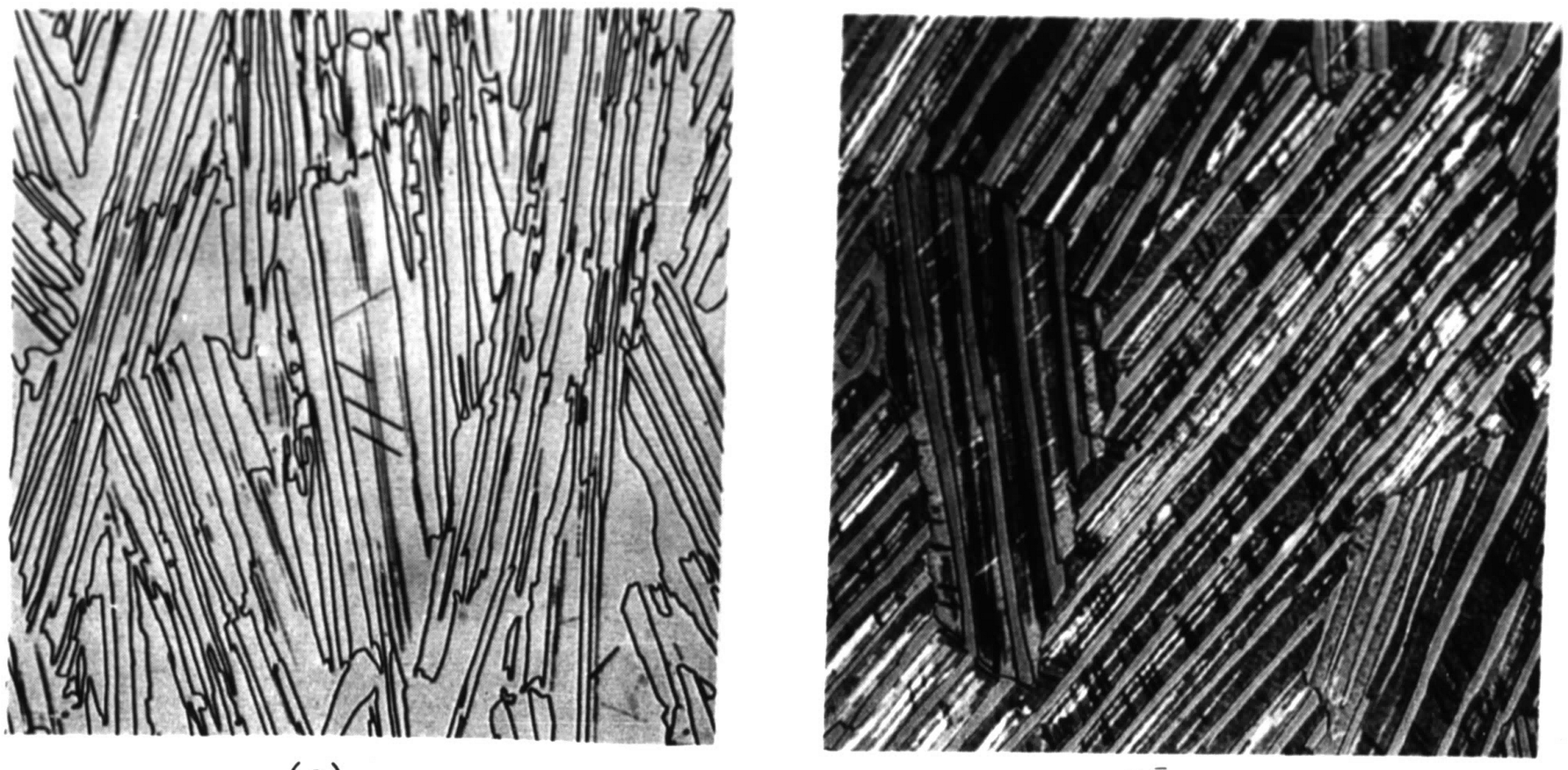

(a) (b)

Figure 3: Photomicrographs illustrating δ phase precipitation of Widmanstatten morphology present after heat treatment.
(a) Aged for 3 hours at 1000°C. 200X.
(b) Solution treated, quenched, and aged for 1 hour at 1000°C. 533X. (Polarized Light)

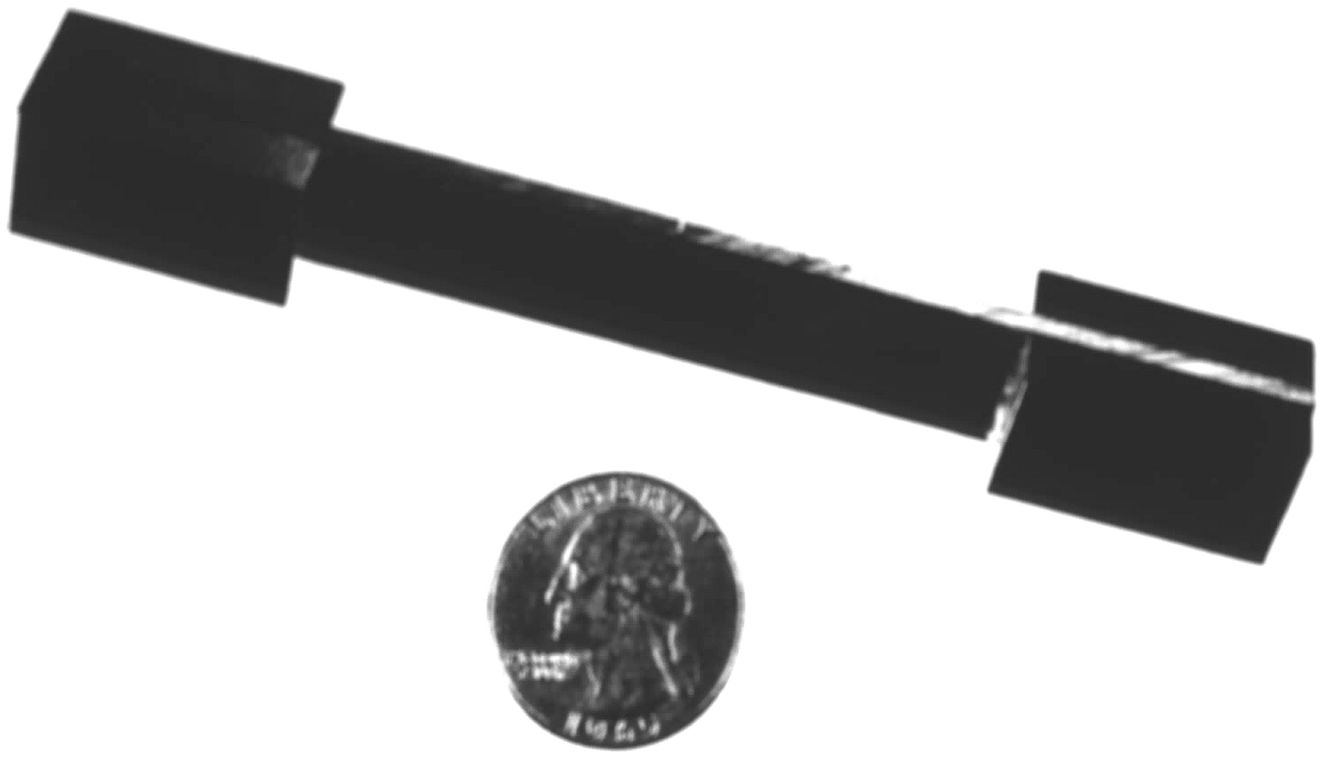

Figure 4: Four-point bending test sample.

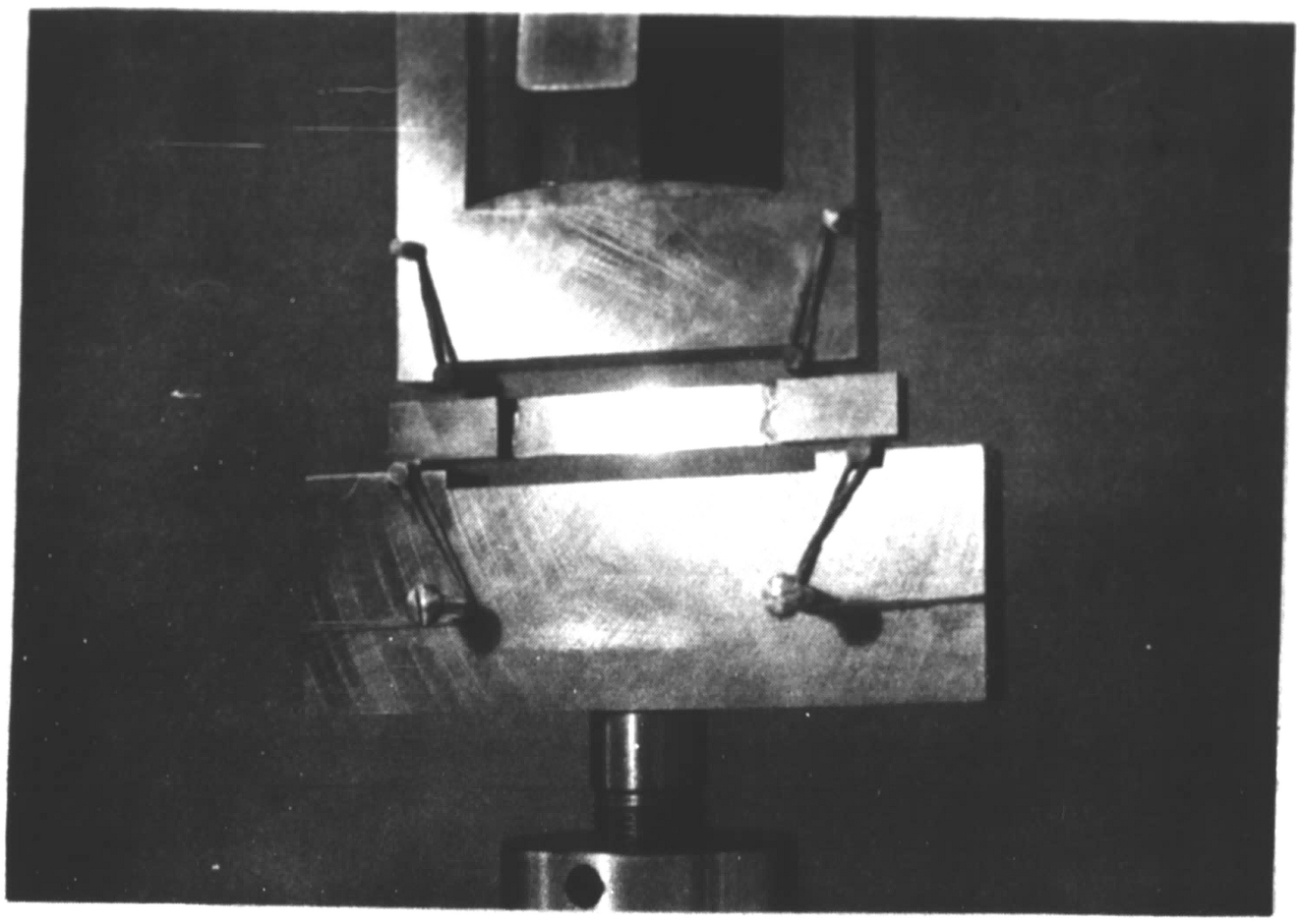

Figure 5: A photograph showing the four-point bending fixture and test sample taken during an actual fatigue test. 1/2X.

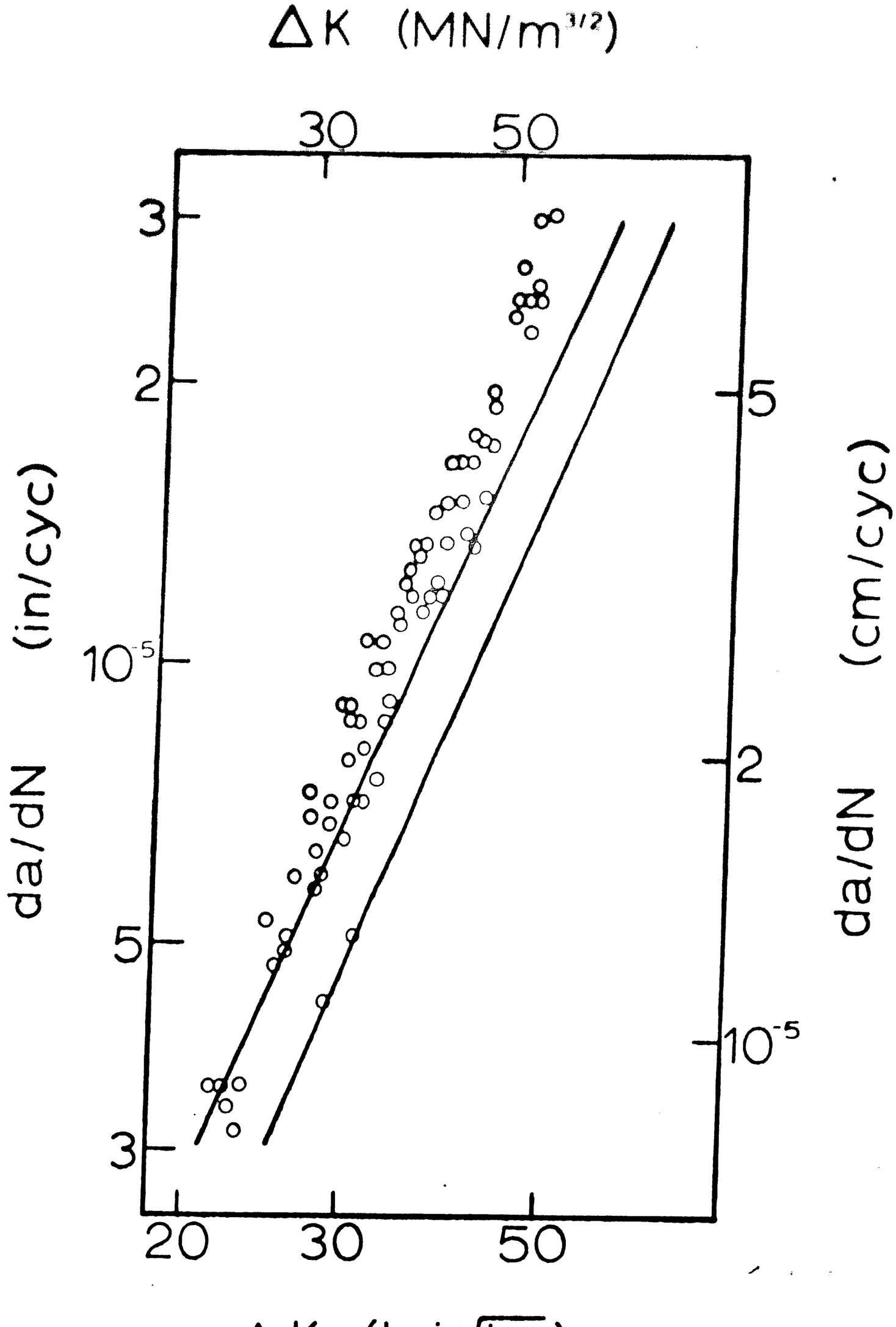


Figure 6: Fatigue crack growth rate vs $\Delta K$ for T-1 steel as compared to previously determined results (data band: 33,34).

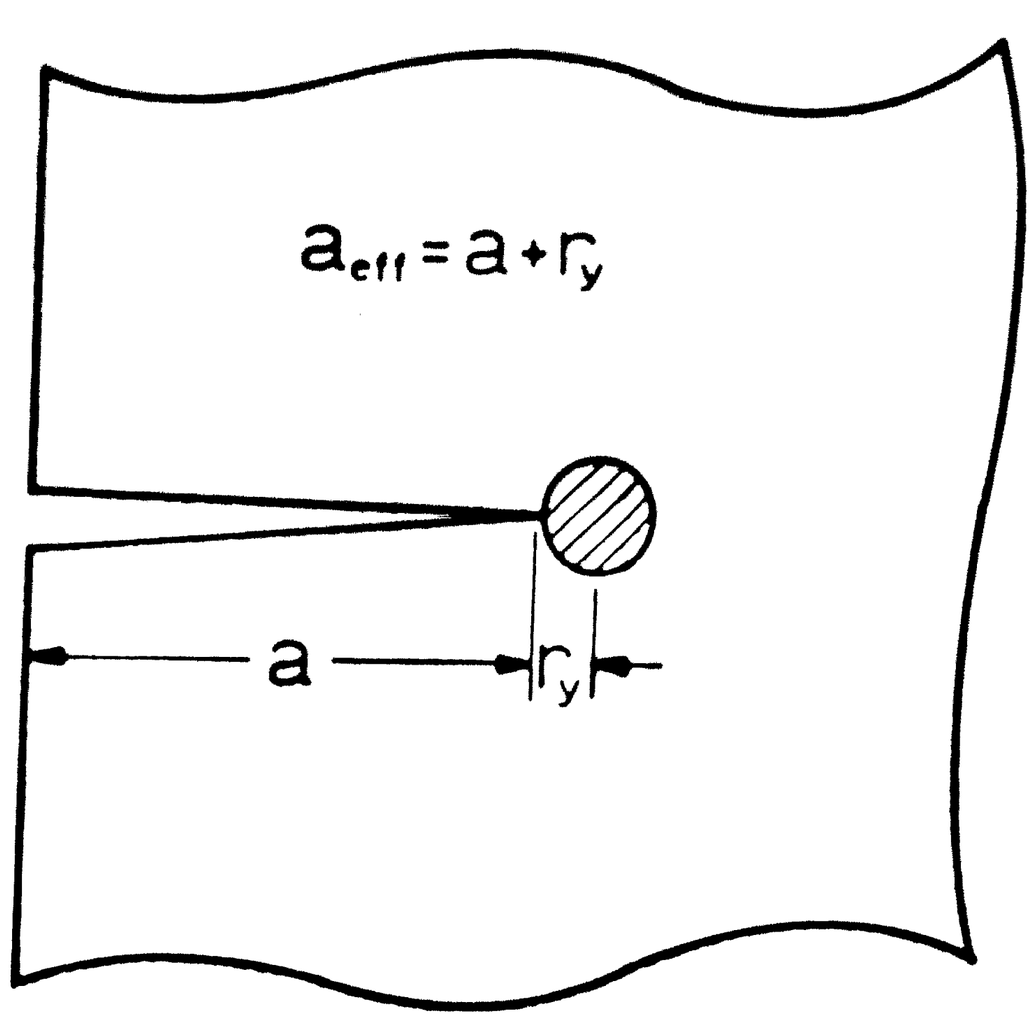


$$K_{eff} = Y\left(\frac{a_{eff}}{W}\right)\sigma\sqrt{\pi a_{eff}}$$

Figure 7: Diagram depicting the plastic zone size that exists ahead of the advancing crack tip.

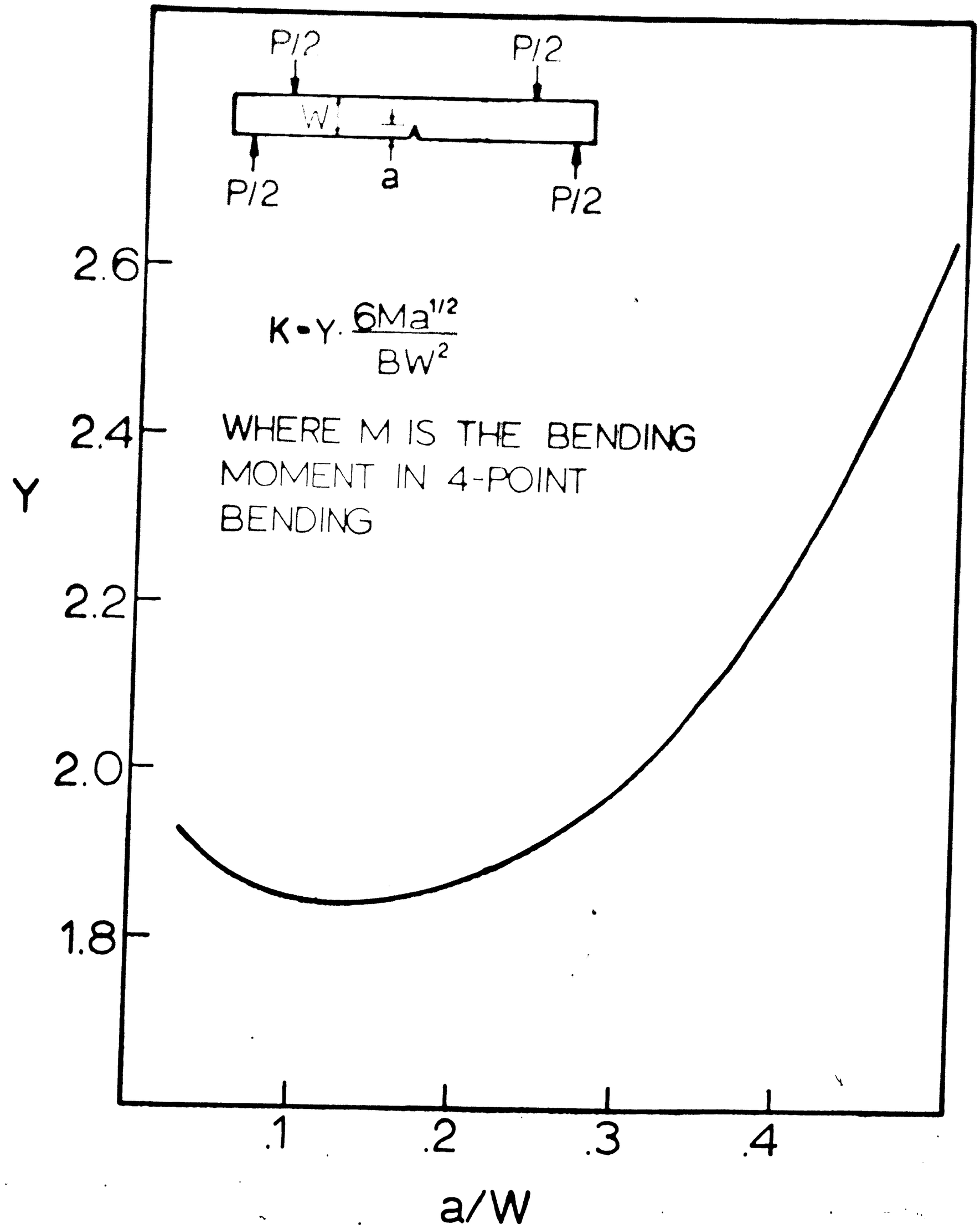


Figure 8: Plot of the geometrical correction factor, Y, as a function of a/W. (35)

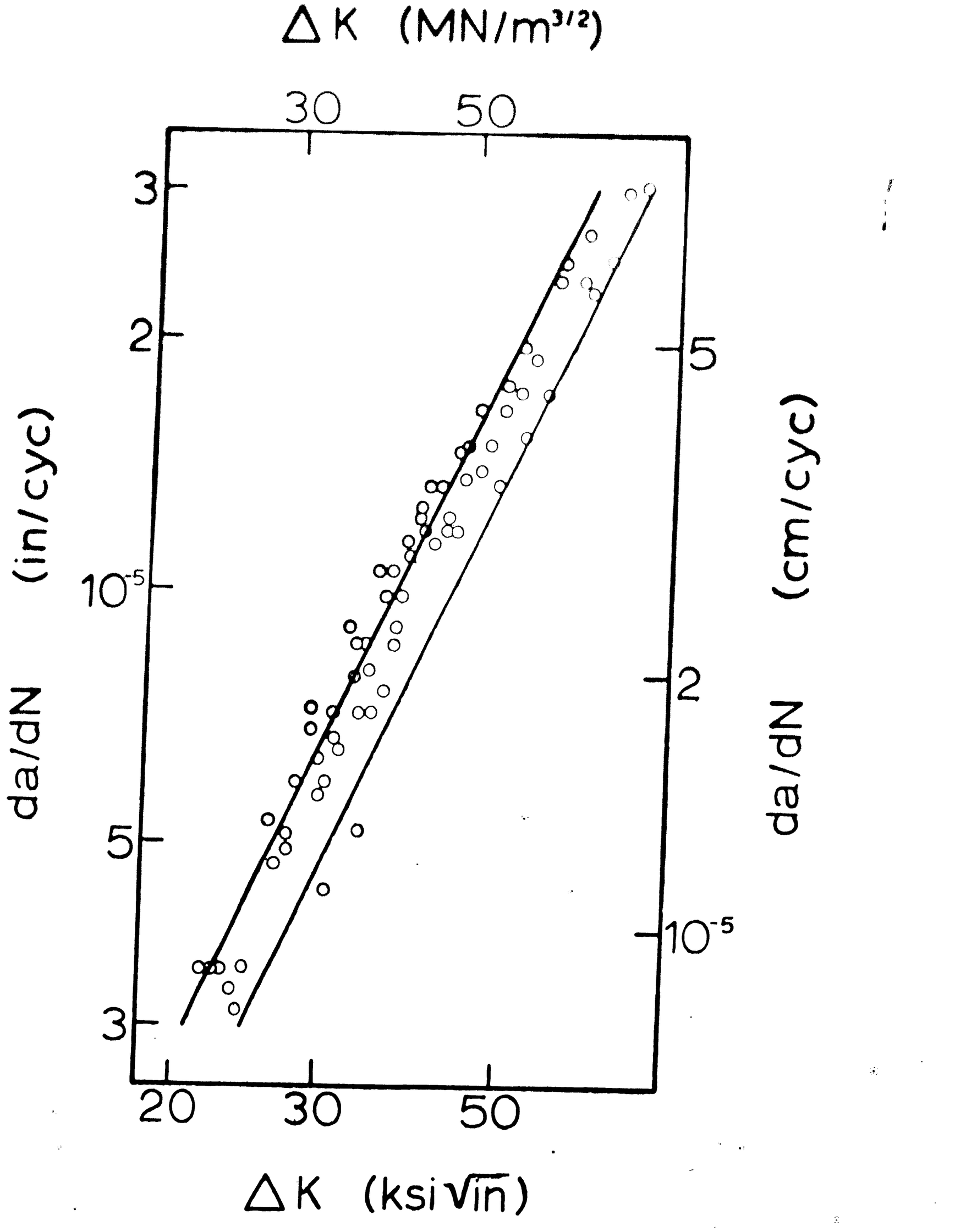


Figure 9: Fatigue crack growth rate vs $\Delta K$ for T-1 steel corrected for plasticity.

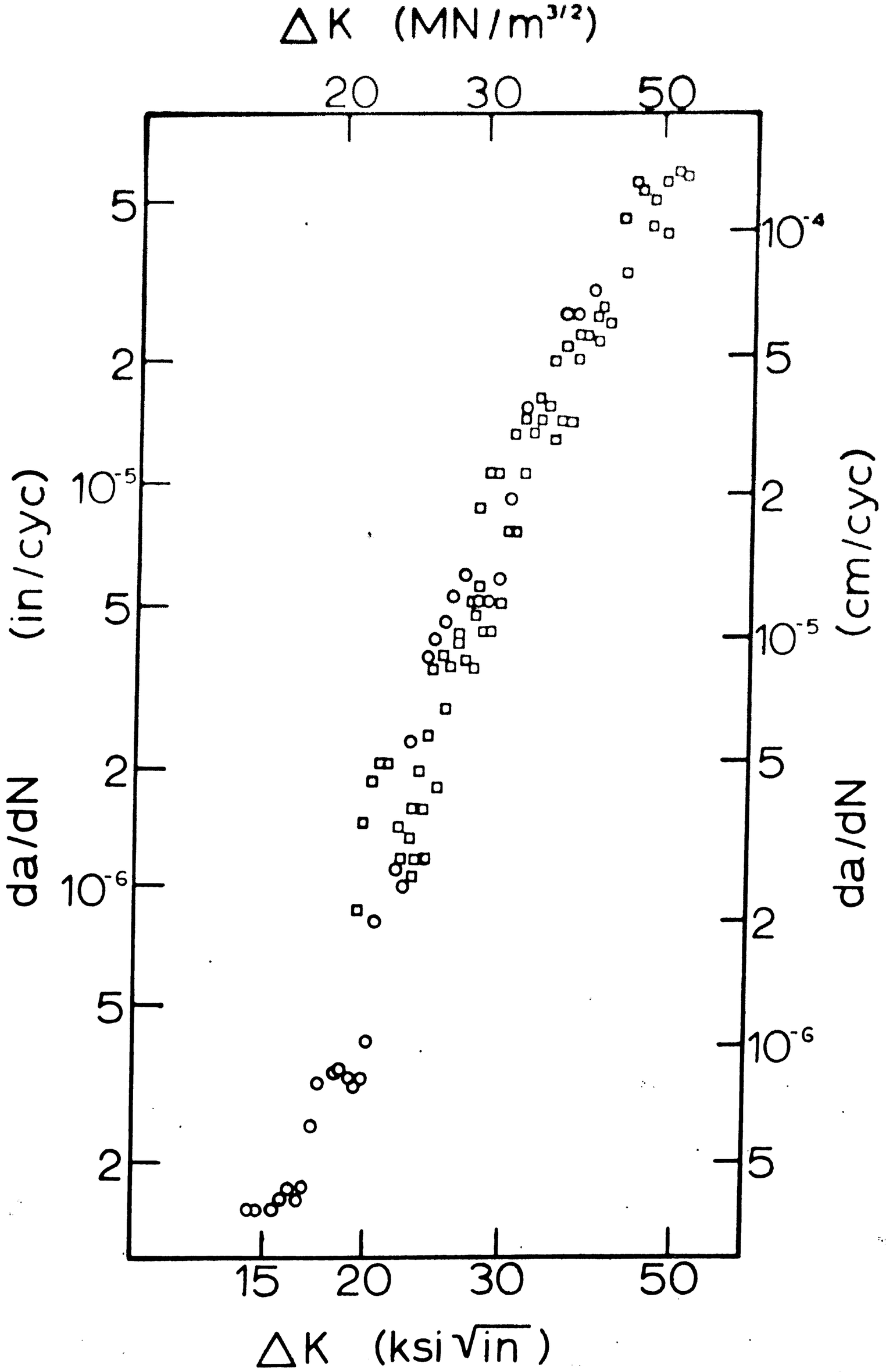


Figure 10: Fatigue crack growth rate vs $\Delta K$ for the Ni-$Ni_3Nb$ eutectic composite ($R < 0.1$). (O : 20 Hz, □ : 10 Hz)

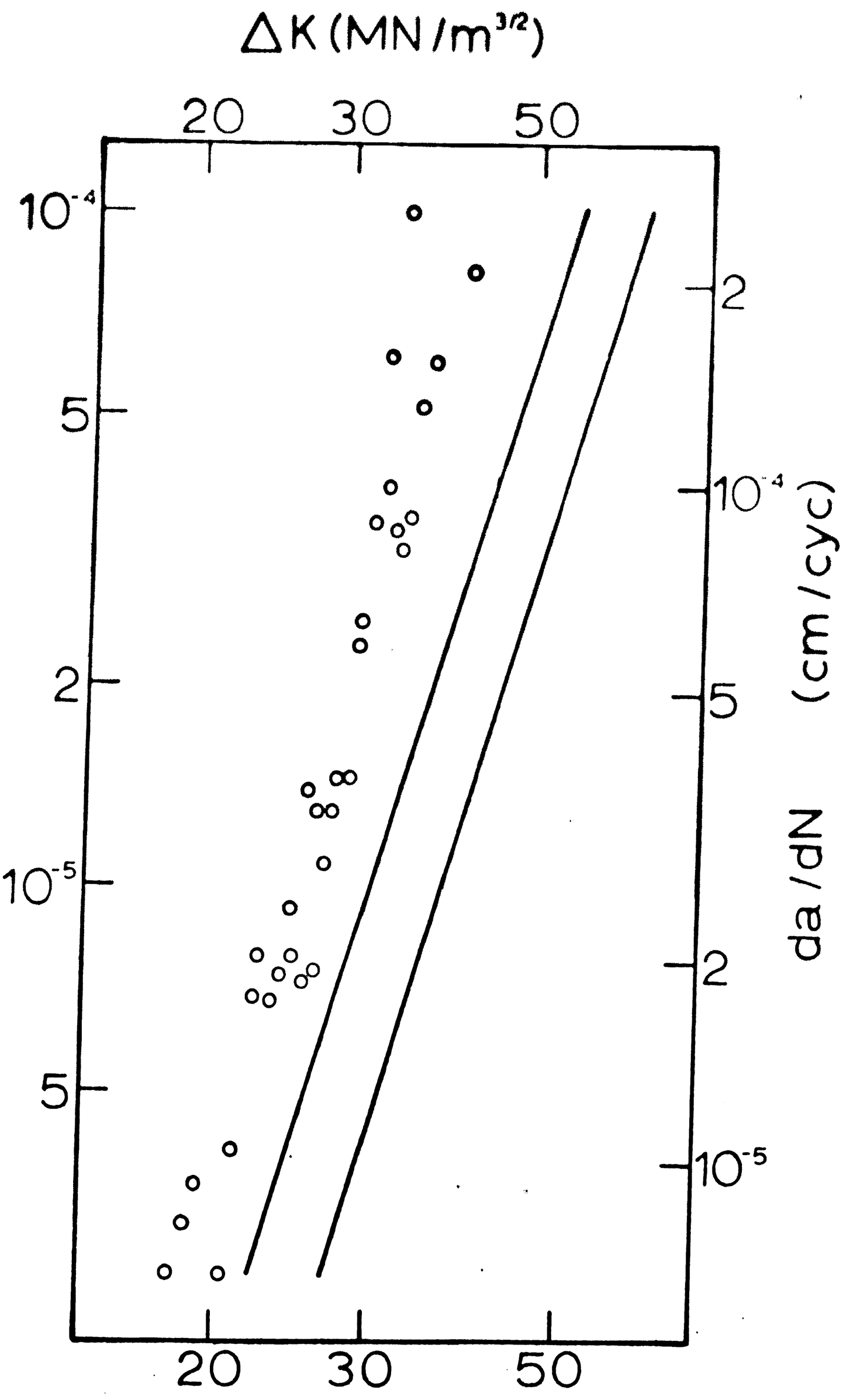


Figure 11: Fatigue crack propagation rates vs $\Delta K$ for the Ni-$Ni_3Nb$ eutectic composite (R = 0.5). Data band represents $R < 0.1$ data range from Figure 10.

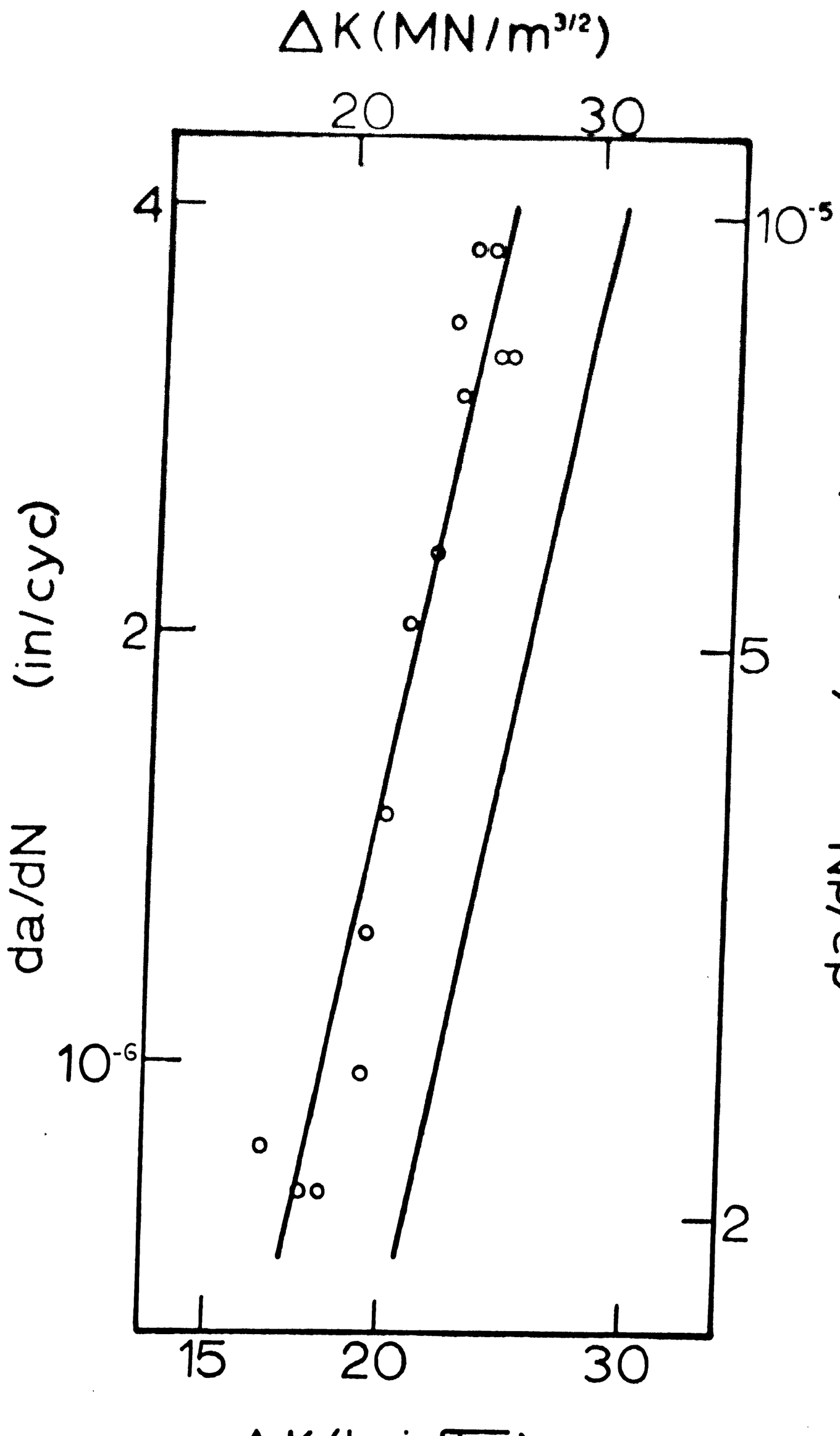


Figure 12: Fatigue crack growth rate vs $\Delta K$ for the Ni-$Ni_3Nb$ eutectic composite in a water environment. Data band represents data range in an air atmosphere taken from Figure 10.

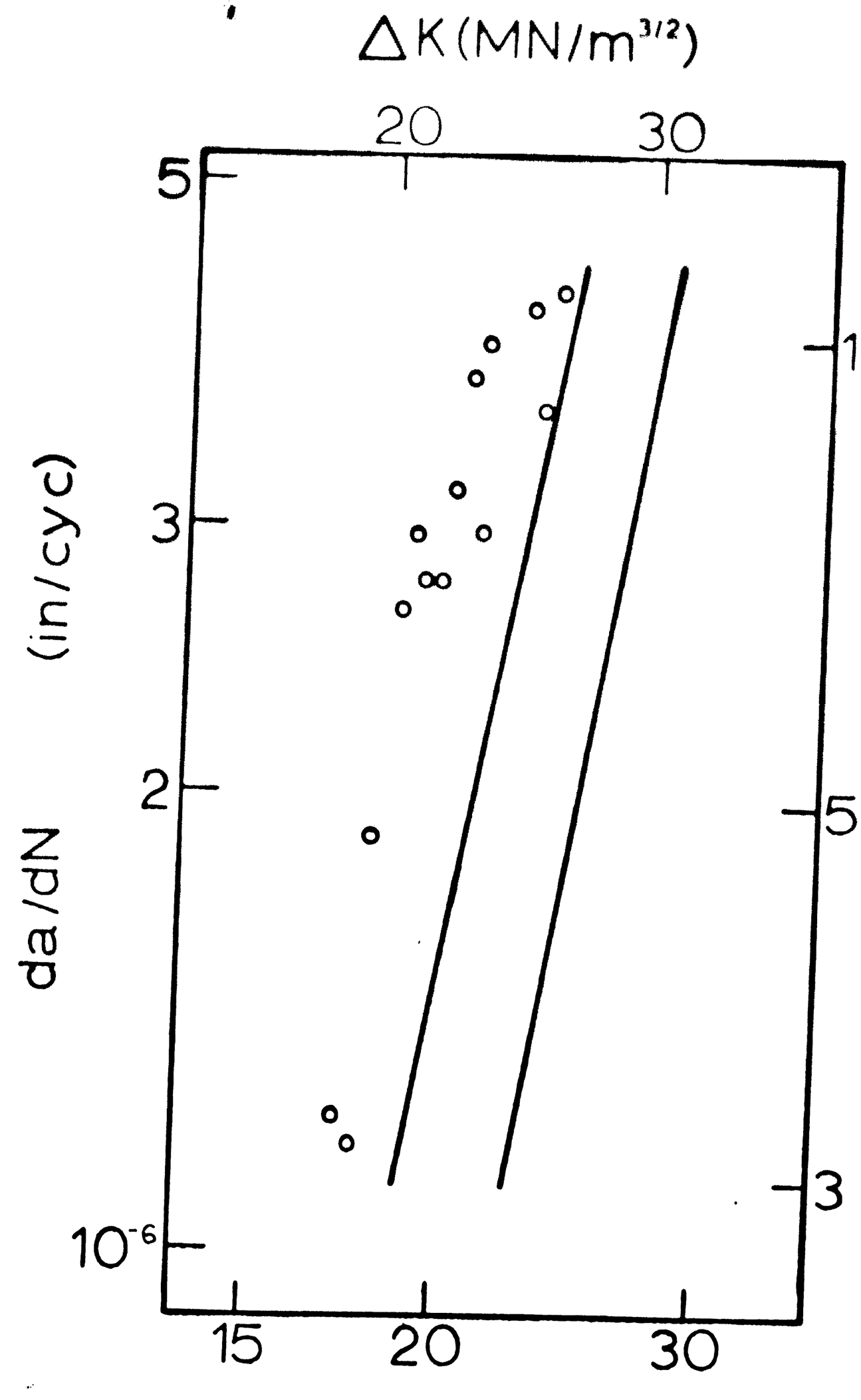


Figure 13: Fatigue crack growth rate vs $\Delta K$ for the non-controlled alloy. Data band represents the data range for the as-controlled composite.

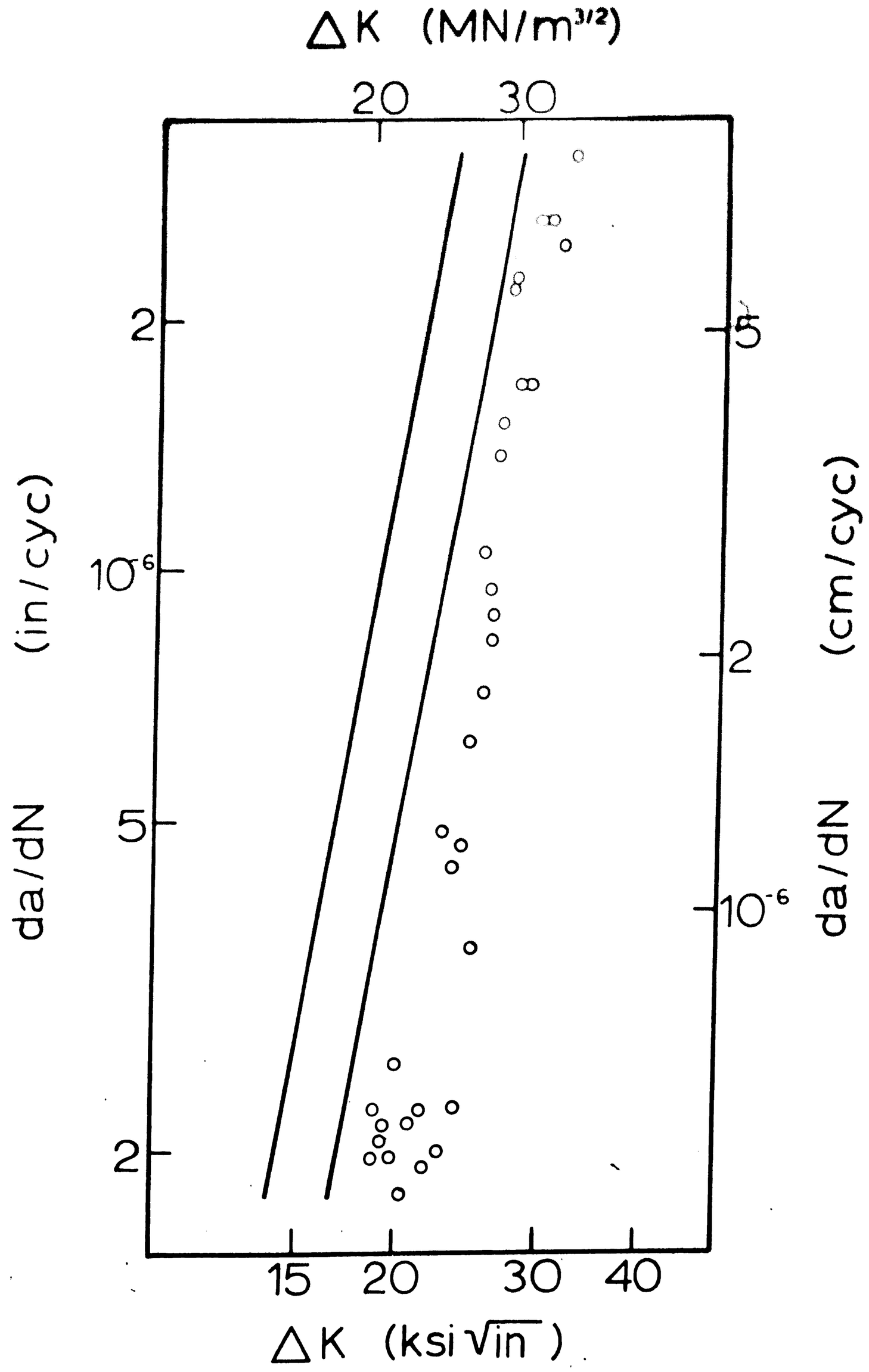


Figure 14: Fatigue crack growth rate vs $\Delta K$ for the age hardened Ni-$Ni_3Nb$ eutectic composite. Data band represents the data range for the as-grown composite.

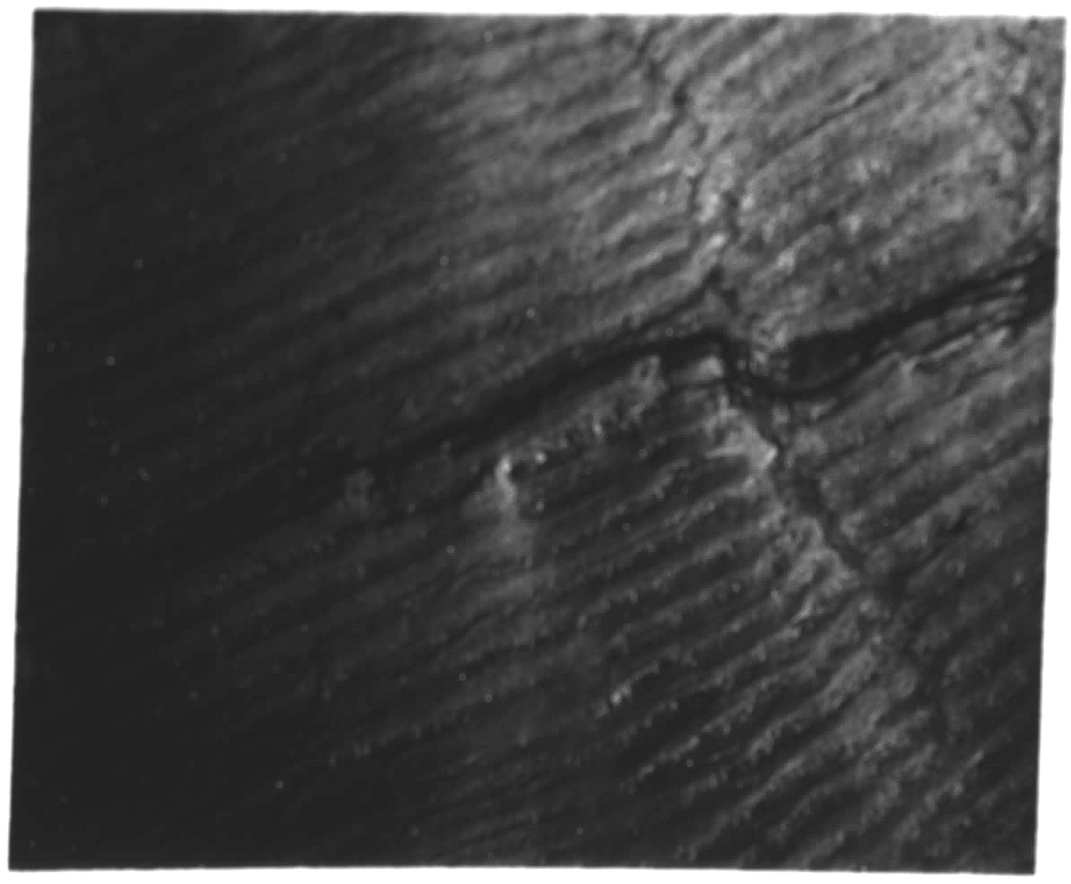

(a)

(b)

Figure 15: Electron fractographs revealing the fracture surface appearance under high $\Delta K$ conditions.
(a) Typical striations found on the $\gamma$ matrix fracture surface. 5300X.
(b) Striations remain parallel to the $\gamma/\delta$ interface irrespective of the $\delta$ platelet orientation. 6600X.

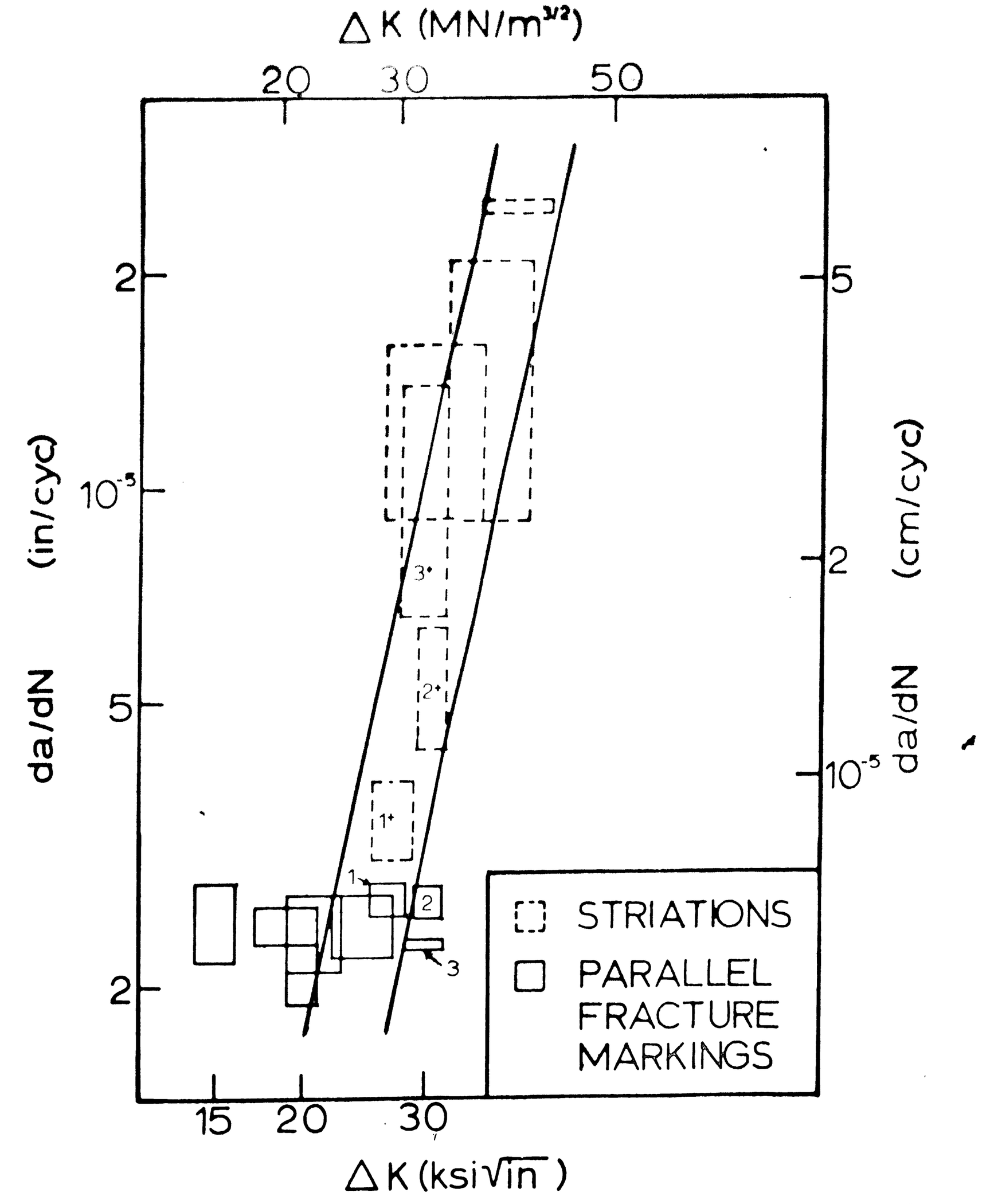


Figure 16: Plot representing the macroscopic (data band) and microscopic (striation spacing, ⬚ ) growth rates of the $Ni-Ni_3Nb$ eutectic composite as a function of $\Delta K$. The solid boxes represent the spacing of the parallel fracture markings found superimposed on the Stage I fracture surface. Boxes labelled 1-1*, 2-2* and 3-3* correspond to the spacing of the parallel fracture markings and the striations, respectively, observed on a given replica.

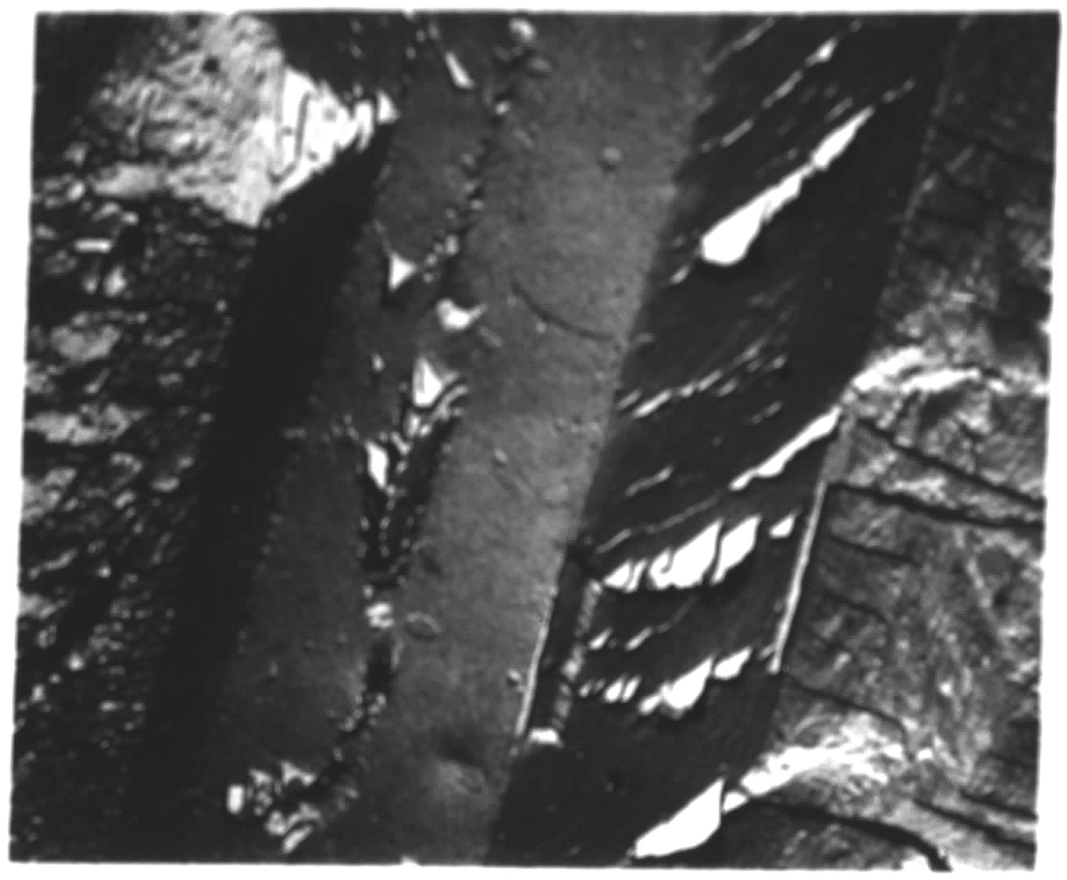

(a)

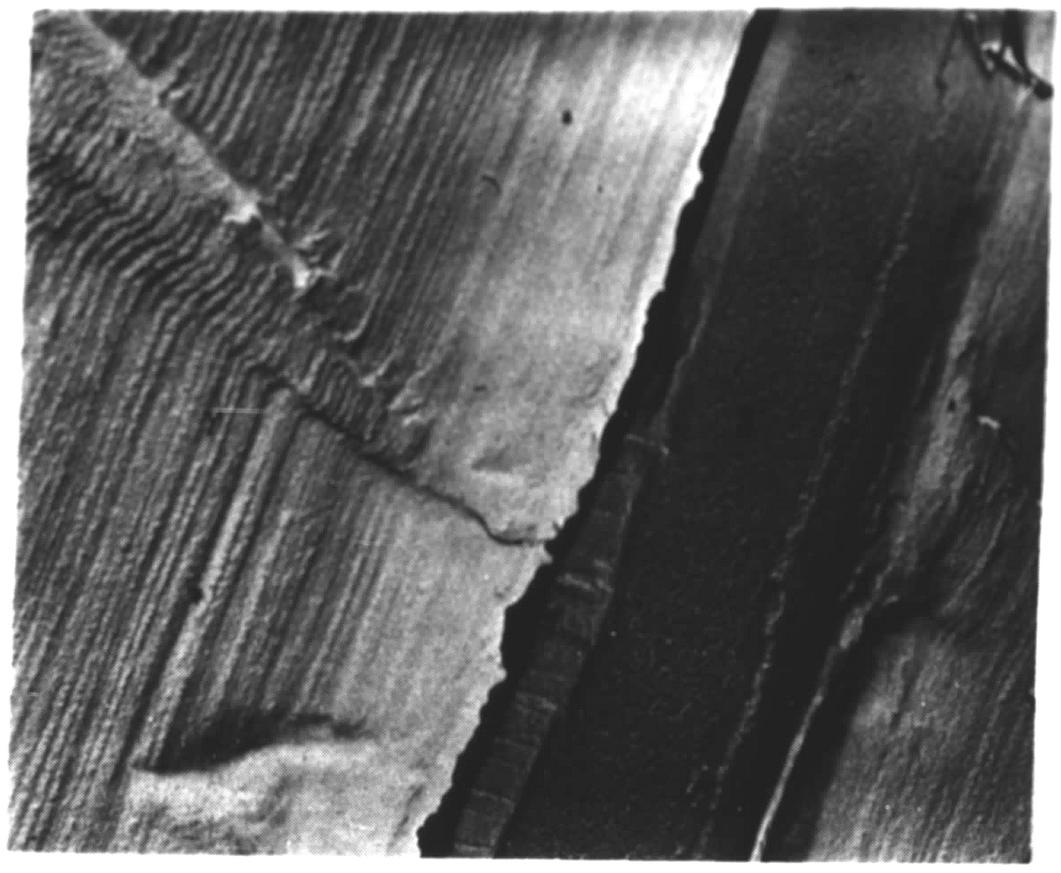

(b)

Figure 17: Electron fractographs of the fracture surface revealing:
(a) Twin related steps and tongues found at the δ fracture surface. 9000X.
(b) A fin along the interphase boundary indicative of delamination. 6600X.

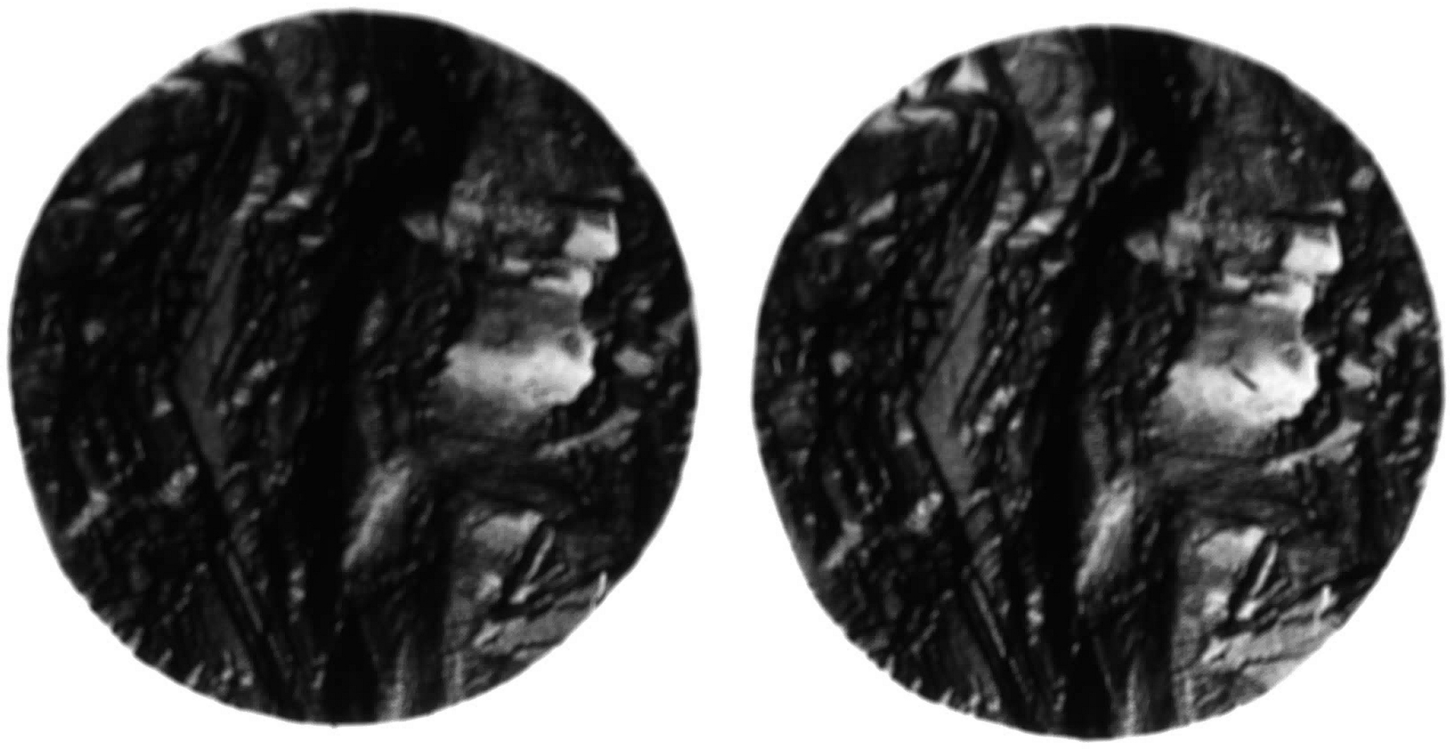

Figure 18: Typical electron fractograph of the low growth rate region showing faceting of the $\gamma$ matrix-stereographic pair. ($\pm 3°$) 6600X.

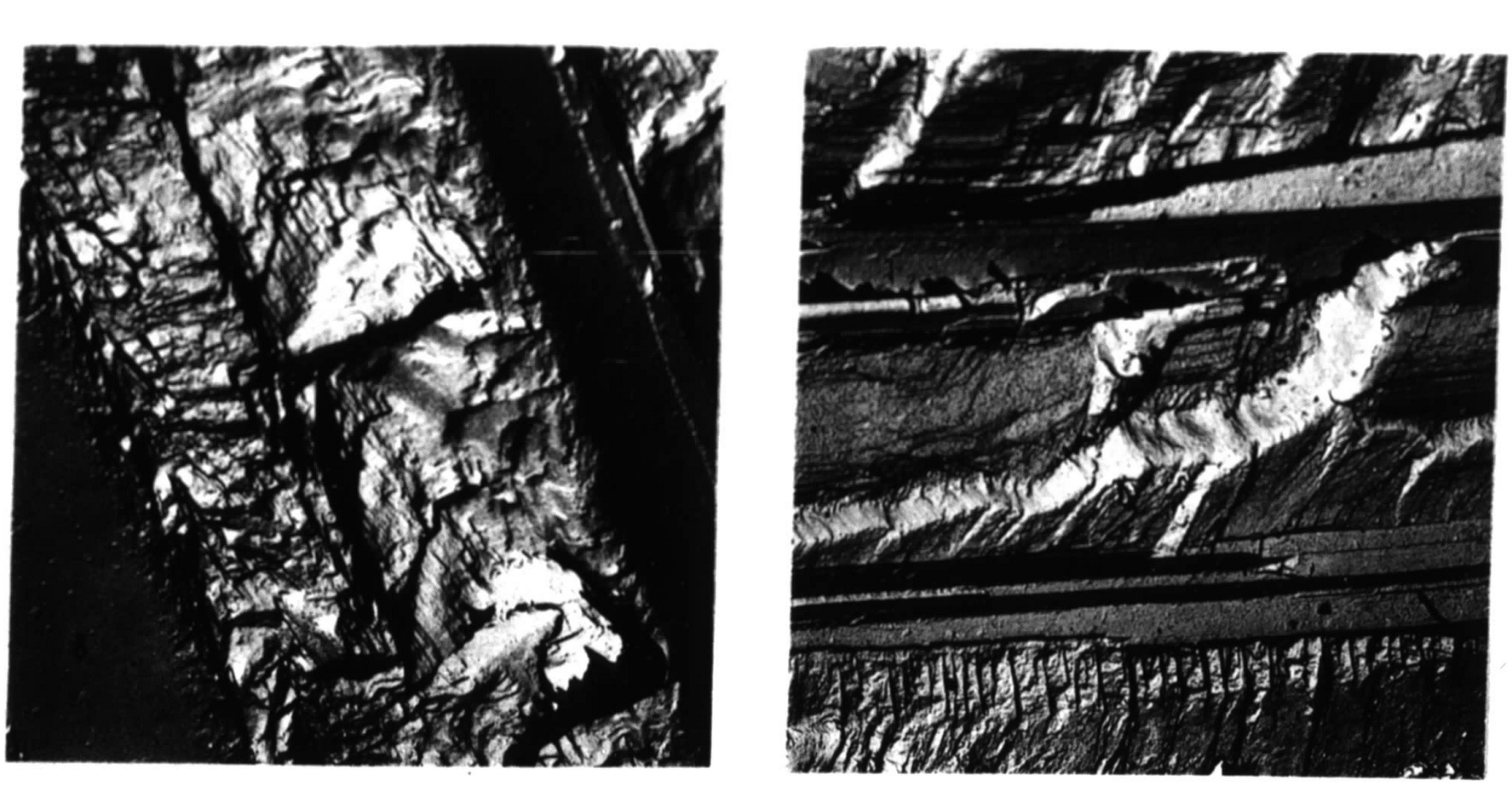


(a) (b)

Figure 19: Electron fractographs revealing the fracture surface appearance under low $\Delta K$ conditions.
(a) Stage I facets on the $\gamma$ fracture surface. 6600X.
(b) Stage I faceting and dark fins present at the interphase boundary indicative of delamination. 5300X.

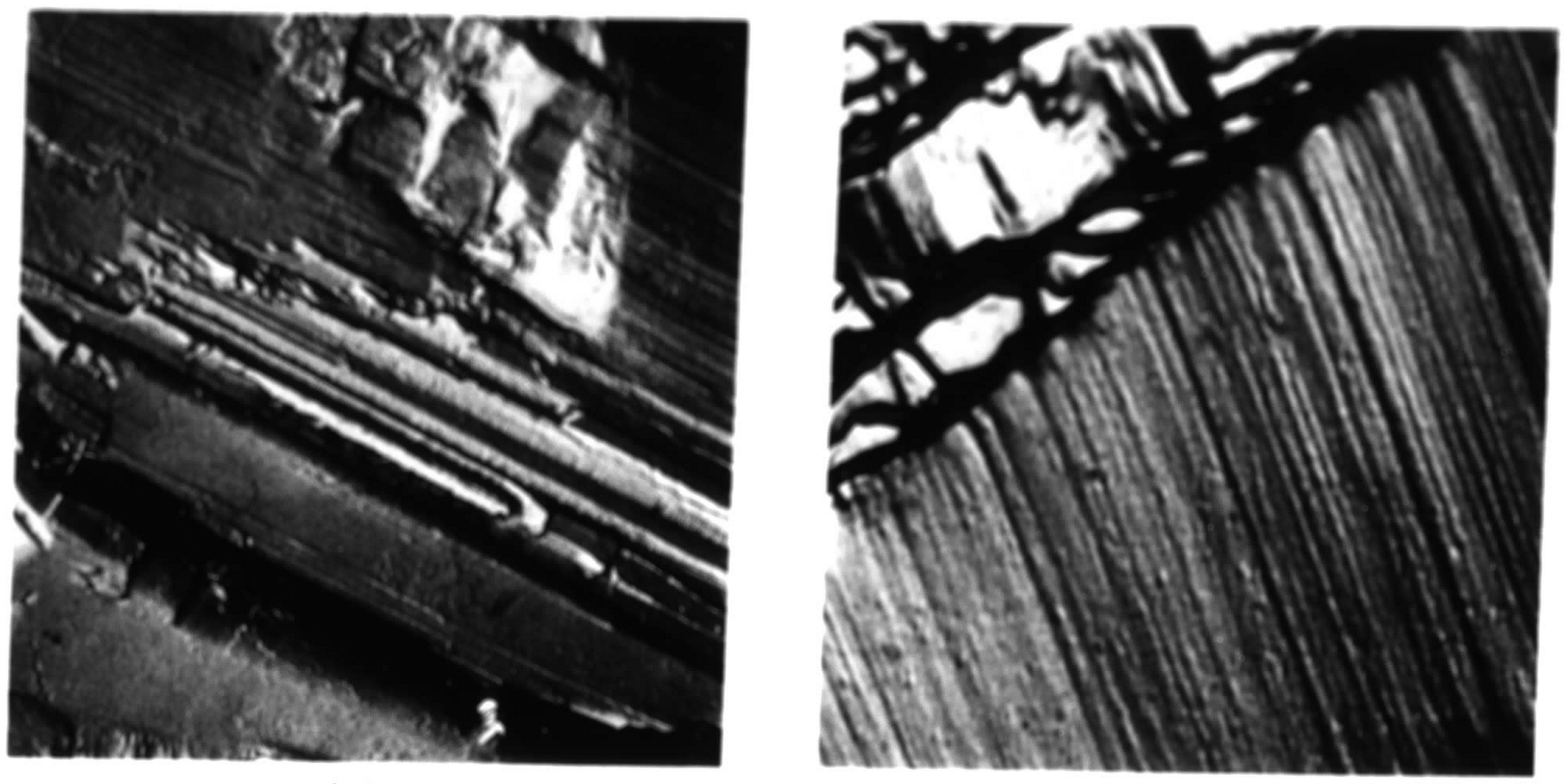

(a) (b)

Figure 20: Electron fractographs revealing parallel fracture markings.
(a) Evidence of fine parallel lines superimposed on the $\gamma$ matrix faceted fracture surface. 10,000X.
(b) Increased magnification of a region containing parallel fracture marking in order to resolve individual lines. (Spacing approximately 600Å) 23,000X.



(a) (b)

Figure 21: Typical electron fractographs of the intermediate growth rate region illustrating:
(a) Poorly defined facets and striations present in the same $\gamma$ phase region. 5600X.
(b) Evidence of serpentine glide on the $\gamma$ matrix fracture surface. 14,000X.

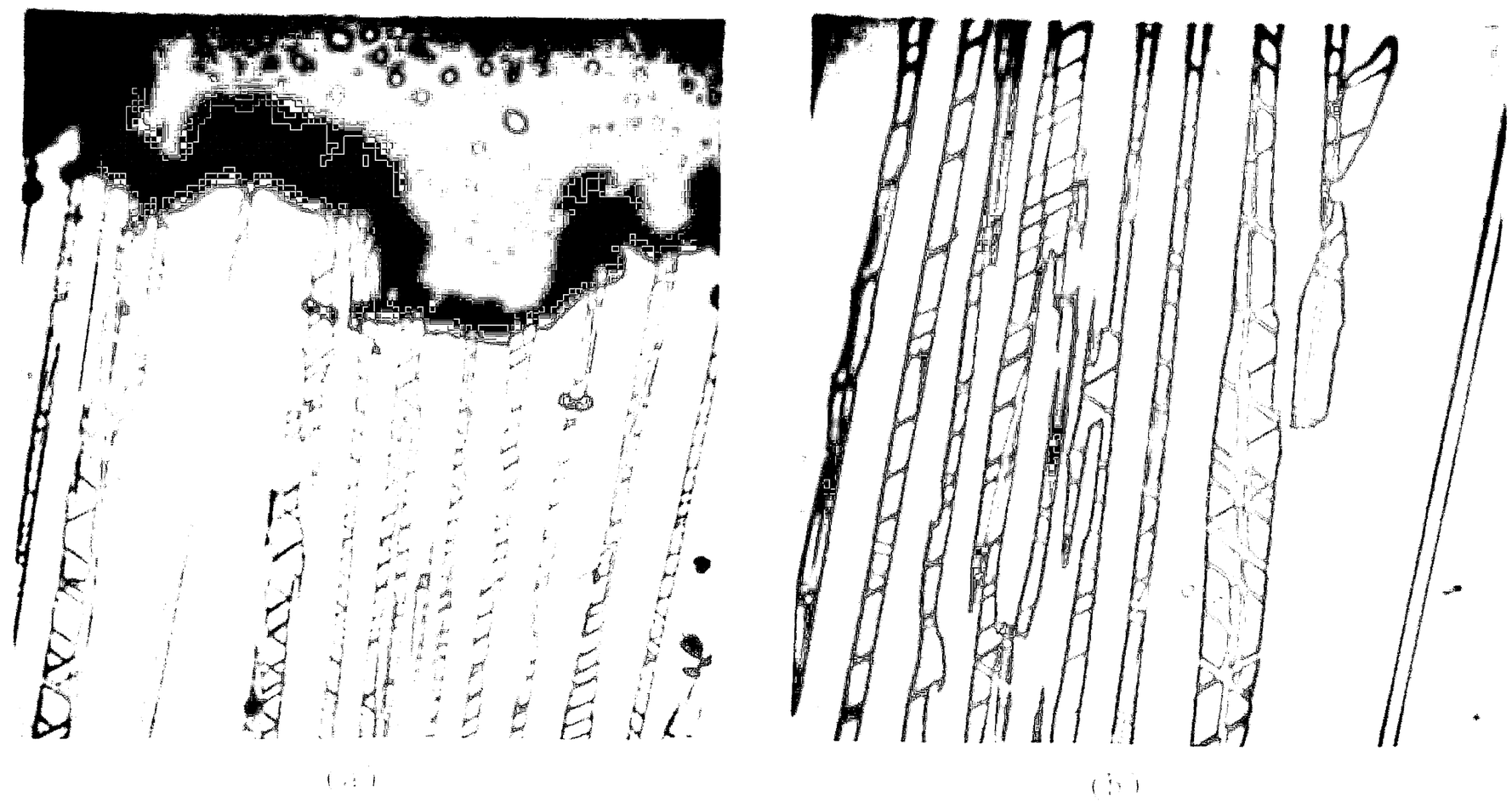

(a) (b)

**Figure 22:** Typical metallographic profile of a fatigue fracture at high growth rates. (Etchant B)
**(a)** {211}$_\gamma$ twinning and subsequent twin boundary cracking near the fracture surface. 533X.
**(b)** {211}$_\gamma$ and {011}$_\gamma$ twinning, the latter appearing approximately parallel to the $\gamma/\delta$ interface. 800X.

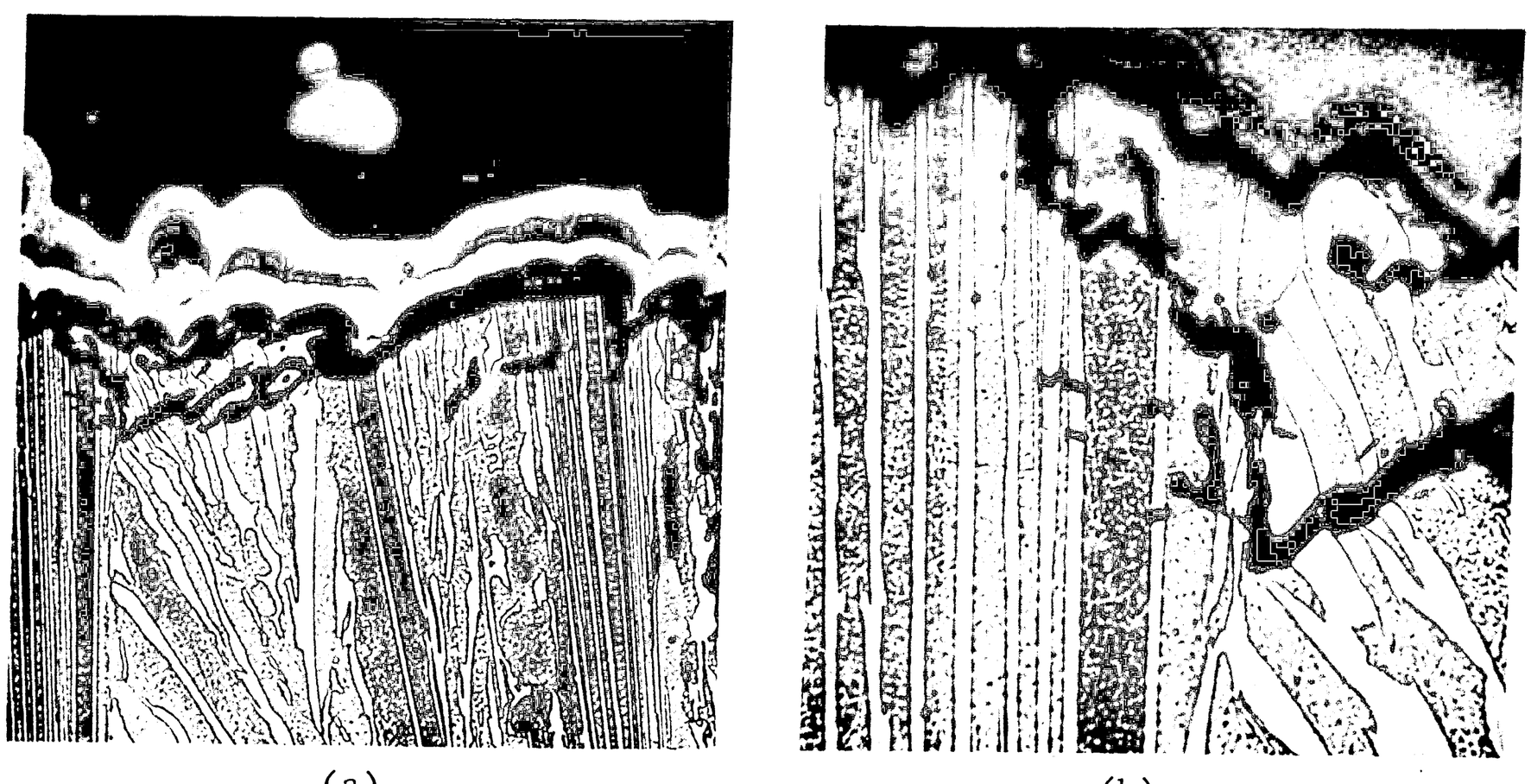

(a) (b)

Figure 23: Typical metallographic profile of a fatigue fracture at low growth rates. (Etchant A)
(a) Secondary fatigue cracks that propagated parallel to the primary fatigue crack. 133X.
(b) Increased magnification of the region at the secondary crack tip where a significant number of $\delta$ platelets have undergone twin boundary cracking in advance of the crack front. 533X.

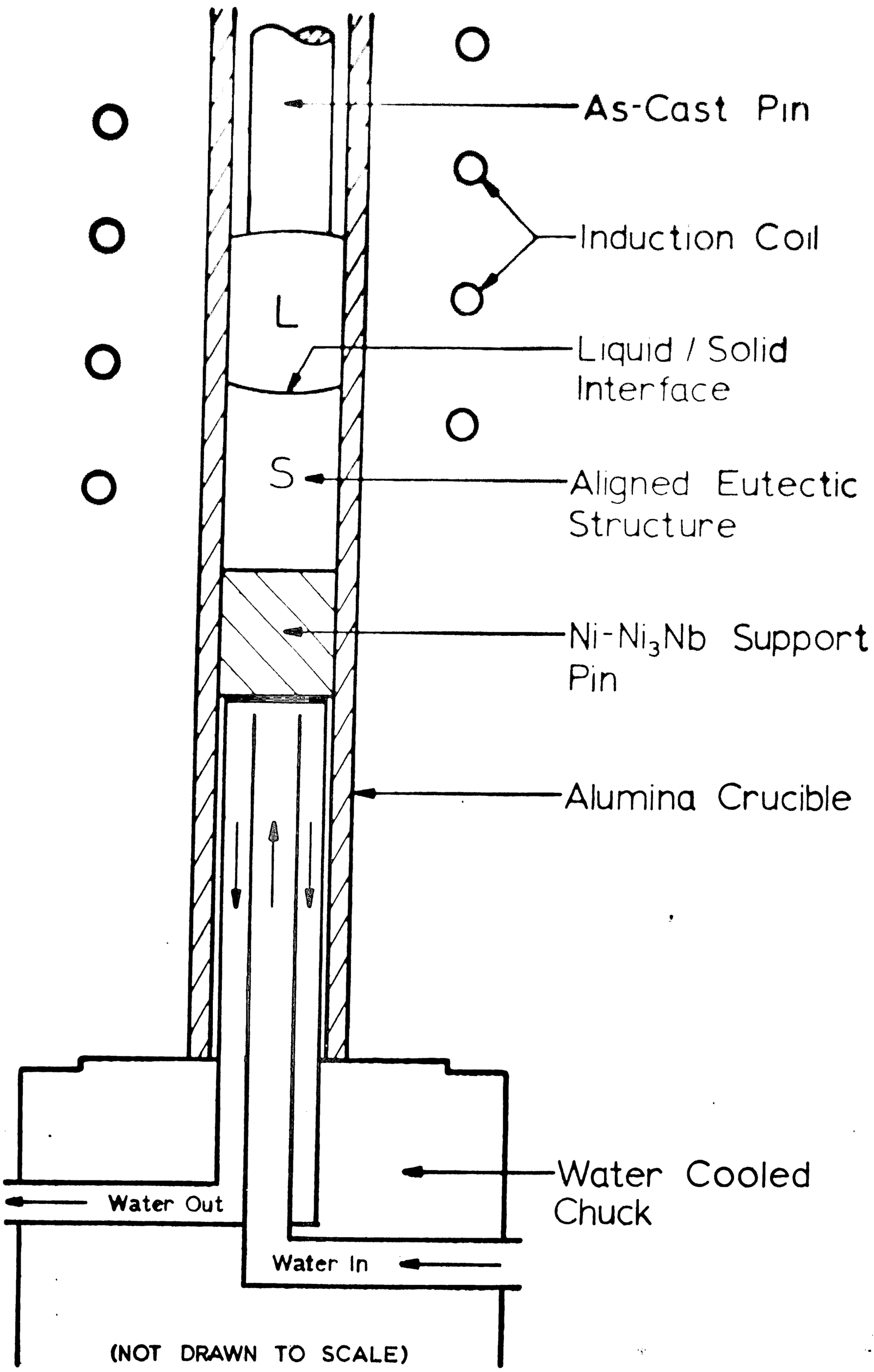


Figure 24: Schematic diagram of unidirectional solidification apparatus.

## REFERENCES


1. L. M. Hogan, R. W. Kraft and F. D. Lemkey: "Eutectic Grains," Advances in Materials Research, vol. 5, p. 83, John Wiley and Sons, Inc., New York, 1971.

2. R. W. Hertzberg: "Potential of Unidirectionally Solidified Eutectic Alloys as Reinforced Composites," Fiber Composite Materials, p. 77, ASM, Metals Park, Ohio, 1965.

3. M. Salkind, G. Leverant and F. George: "Stability of Eutectic Composites Stressed at Elevated Temperatures," J. Inst. Met., 1967, vol. 95, p. 349.

4. L. D. Graham and R. W. Kraft: "Coarsening of Eutectic Microstructures at Elevated Temperatures," Trans. AIME, 1966, vol. 236, p. 94.

5. R. W. Kraft, D. L. Albright and J. A. Ford: "Anomalous Thermal Stability of Al-$CuAl_2$ Eutectic Specimens," Trans. AIME, 1963, vol. 227, p. 540.

6. E. R. Thompson and E. H. Kraft, and F. D. George: "Investigation to Develop a High Strength Eutectic for Aircraft Engine Use," Final Report, Contract N00019-71-C-0096, United Aircraft Research Laboratories, July 31, 1971.

7. E. R. Thompson and F. D. Lemky: "Unidirectional Solidification of Co-Cr-C Monovariant Eutectic Alloys," Met. Trans., 1970, vol. 1, p. 2799.

8. F. D. Lemkey: "Developing Directionally Solidified Eutectics for Use Up to 1235°C," United Aircraft Research Laboratories, First Quarterly Report, Contract NAS3-15562, 1971.

9. R. T. Quinn: Structure and Elevated-Temperature Mechanical Behavior of Unidirectionally Solidified Ni-$Ni_3Nb$ Eutectic Alloy, Ph.D. Dissertation, Lehigh University, 1967.

10. R. T. Quinn, R. W. Kraft and R. W. Hertzberg: "Structure and Elevated-Temperature Mechanical Behavior of Unidirectionally Solidified Ni-$Ni_3Nb$ Eutectic Alloy," Trans. ASM, 1969, vol. 62 p. 38.

11. W. R. Hoover: The Monotonic and Cyclic Mechanical Response of the Ni-$Ni_3Nb$ Eutectic Composite, Ph.D. Dissertation, Lehigh University, 1970.

12. W. R. Hoover and R. W. Hertzberg: "The Mechanical Response of the Ni-$Ni_3Nb$ Eutectic Composite: Part I. Monotonic Behavior," Met. Trans., 1971, vol. 2, p. 1283.

13. W. R. Hoover and R. W. Hertzberg: "The Mechanical Response of the Ni-$Ni_3Nb$ Eutectic Composite: Part II. Cyclic Behavior," Met. Trans., 1971, vol. 2, p. 1289.

14. R. P. Gangloff: Elevated Temperature Tensile and Creep Rupture Behavior of Unidirectionally Solidified Ni-$Ni_3Nb$ Eutectic Composite, Master's Thesis, Lehigh University, 1972.

15. P. Annamuma and M. Turpin: "Structure and High Temperature Mechanical Behavior of Ni-$Ni_3Nb$ Unidirectional Eutectic," Met. Trans., 1972, vol. 3, p. 137.

16. D. Senicourt and P. Annanmma: "Structure et Cristallographie de l'Eutectique Orienta Ni-$Ni_3Nb$," C. R. Acad. Sc., Serie C, 1969, vol. 269, p. 591.

17. C. Grossiord, G. Lesoult and M. Turpin: "Slip and Mechanical Twinning in Ni-$Ni_3Nb$ Directionally Solidified Eutectic Alloy," Electron Microscopy and Structure of Materials, p. 678, University of California Press, Berkeley, 1972.

18. C. Grossiord and M. Turpin: "Deformation Twins in the $Ni_3Nb$ Phase," Met. Trans.,1973, vol. 4, p. 1415.

19. I. J. Dueden and W. Hume-Rothery: "The Equilibrium Diagram of the System Niobium-Nickel," J. Less-Common Metals, 1966, vol. 11, p. 381.

20. M. J. Salkind, F. D. George, F. D. Lemkey and B. J. Bayles: "An Investigation of the Creep, Fatigue and Transverse Properties of $Al_3Ni$ Whiskers and $CuAl_2$ Platelet Reinforced Aluminum," United Aircraft Research Laboratories, Final Report, Contract NOw65-0384-d, 1966.

21. W. R. Hoover and R. W. Hertzberg: "The Fatigue Characteristics of Unidirectionally Solidified Al-$Al_3Ni$ Eutectic Alloy," Trans. ASM, 1968, vol. 61, p. 769.

22. W. G. Ovens, Jr. and A. J. McEvily, Jr.: "Fatigue Behavior in Torsion of an Unidirectionally Solidified Eutectic," Conference on In Situ Composites, vol. 2, p. 273, Publication NMAB-308-11, National Academy of Sciences-National Academy of Engineering, Washington, D. C., 1973.

23. R. Kossowsky, K. Sadananda and M. Doner: "Fatigue Deformation in Ni-Cr Lamellar Composites," Electron Microscopy and Structure of Materials, p. 764, University of California Press, Berkeley, 1972.

24. A. R. T. de Silva and G. A. Chadwick: "The Fatigue Behavior of the Unidirectionally Solidified Fibrous Fe-$Fe_2B$ Eutectic Alloy," Metal Sci. J., 1970, vol. 4, p. 61.

25. E. R. Thompson, E. E. Kraft and F. D. George: "Investigation to Develop a High Strength Eutectic for Aircraft Engine Use," United Aircraft Research Laboratories, Final Report, Contract N00019-71-C-0096, 1971.

26. M. F. Henry: "Low Cycle Fatigue of the Directionally Solidified Eutectic Ni(Cr)-TaC," paper presented at the 1973 Spring Meeting of The Metallurgical Society of AIME.

27. A. Forero Mora: Solid State Bonding of Directionally Solidified Ni-$Ni_3Nb$ Eutectic Alloy, Master's Thesis, Lehigh University, 1972.

28. K. A. Hill: Microstructure and Joining of Ni-$Ni_3Nb$ Unidirectionally Solidified Eutectic Composite, Master's Thesis, Lehigh University, 1973.

29. C. G. Rhodes and G. Garmong: "The Aging Response of Al-Cu and Al-Cu-Mg Directionally Soldified Eutectics," Met. Trans., 1972, vol. 3, p. 1861.

30. P. C. Paris: "The Fracture Mechanics Approach to Fatigue," Fatigue-An Interdisciplinary Approach, p. 107, Syracuse University Press, Syracuse, New York, 1964.

31. P. Paris and F. Erdogan: "A Critical Analysis of Crack Propagation Laws," J. Basic Eng. Trans. ASME, Series D, vol. 85, 1963, p. 528.

32. M. Ronay: "Fatigue of High-Strength Materials," Fracture, An Advanced Treatise, p. 431, vol. 3, Academic Press, New York, 1971.

33. M. O. Parry: Fatigue Crack Propagation in Welded Structural Steel, Master's Thesis, Lehigh University, 1971.

34. M. Parry, H. Nordberg and R. W. Hertzberg: "Fatigue Crack Propagation in A514 Base Plate and Welded Joints," American Welding Society, Research Supplement, 1972.

35. Plane Strain Crack Toughness Testing of High Strength Metallic Materials, ASTM Special Technical Publication No. 410, Philadelphia, 1967.

36. S. Pearson: "Fatigue Crack Propagation in Metals," Nature, 1966, vol. 211, p. 1077.

37. J. H. Weber, Jr.: Effects of Crystallography of Thermo-Mechanical Treatment on Fatigue Crack Propagation, Ph.D. Dissertation, Lehigh University, 1969.

38. P. J. E. Forsyth: "A Two Stage Process of Fatigue Crack Growth," Proceedings of the Crack Propagation Symposium, p. 76, vol. 1, Cranfield, 1961.

39. P. J. E. Forsyth and C. A. Stubbington: "On the Metallography and Crystallography of Shear Mode Fatigue Fracture in Aluminum Alloys," Metallurgia, 1966, vol. 74, p. 15.

40. R. W. Hertzberg: Application of Electron Fractography and Fracture Mechanics to Fatigue Crack Propagation in High Strength Aluminum Alloys, Ph.D. Dissertation, Lehigh University, 1965.

41. R. W. Hertzberg: "Fatigue Fracture Surface Appearance," Fatigue Crack Propagation, ASTM STP415, Am. Soc. Testing Mats., 1968, p. 89.

42. R. W. Hertzberg and P. C. Paris: "Application of Electron Fractography and Fracture Mechanics to Fatigue Crack Propagation," Proceedings of International Fatigue Conference, Sendai, Japan, 1965, vol. 1, p. 459.

43. A. J. McEvily, Jr. and R. C. Boettner: "On Fatigue Crack Propagation in FCC Metals," Acta Met., 1963, vol. 11, p. 725.

44. H. I. Kaplan and C. Laird: "On the Mechanism of Stage I Crack Propagation in Fatigue," Trans. AIME, 1967, vol. 239, p. 1017.

45. C. Laird: "The Influence of Metallurgical Structure on the Mechanisms of Fatigue Crack Propagation," Fatigue Crack Propagation, ASTM STP 415, Am. Soc. Testing Mats., 1967, p. 131.

46. M. Gell and G. R. Leverant: "The Characteristics of Stage I Fatigue Fracture in a High-strength Nickel Alloy," Acta Met., 1968, vol. 16, p. 553.

47. M. Gell and G. R. Leverant: "The Fatigue of the Nickel-Base Superalloy, Mar-M200, in Single-Crystal and Columnar-Grained Forms at Room Temperature," Trans. AIME, 1968, vol. 242, p. 1869.

48. M. Gell and G. R. Leverant: "The Effect of Temperature on Fatigue Fracture in a Directionally-Solidified Nickel-Base Superalloy," [Proc. Second Internat. Conference on] Fracture, Brighton, 1969.

49. P. J. E. Forsyth and D. A. Ryder: "Fatigue Fracture" Aircraft Engineering, 1960, vol. 32, no. 374, p. 96.

50. C. A. Stubblington: "Some Observations on Air and Corrosion Fatigue on an Aluminum-7.5% Zinc-2.5% Magnesium Alloy," Metallurgia, 1963, vol. 68, p. 109.

51. C. Laird and G. C. Smith: "Crack Propagation in High Stress Fatigue," Phil. Mag., 1962, vol. 7, p. 847.

52. R. C. Bates and W. G. Clark, Jr.: "Fractography and Fracture Mechanics," Trans. ASM, 1969, vol. 62, p. 380.

53. R. K. Ham and M. L. Wayman: "The Fatigue and Tensile Fracture of TD-Nickel," Trans. AIME, 1967, vol. 239, p. 721.

54. C. D. Beachem and D. A. Meyn: Illustrated Glossary of Fractographic Terms, U.S. Naval Research Laboratory, Washington, D. C., NRL Memorandum Report 1547, 1964.

55. C. D. Beachem and D. A. Meyn: "Fracture by Microscopic Plastic Deformation Processes," Electron Fractography, ASTM STP 436, Am. Soc. Testing Mats., 1968, p. 59.

56. P. C. Gallagher: "The Influence of Alloying Temperature and Related Effects on the Stacking Fault Energy," Met. Trans., 1970, vol. 1, p. 2429.

57. R. T. DeHoff and F. N. Rhines: Quantitative Microscopy, McGraw-Hill, New York, 1968.

58. E. E. Underwood: Quantitative Stereology, Addison-Wesley, Reading, Mass., 1970.

59. I. Miller and J. E. Freund: Probability and Statistics for Engineers, Prentice-Hall, Englewood Cliffs, New Jersey, 1965.

## Appendix I: EXPERIMENTAL PROCEDURES

### Solidification

Solidification techniques employed in producing unidirectionally solidified ingots during the current investigation were similar to the procedures described by Hoover (11) and Gangloff (14). 2000 gram master heats of Ni-23 weight percent Nb using high purity starting material (99.95 percent Ni and 99.87 percent Nb) were induction melted in an $Al_2O_3$ crucible under a vacuum purged, positive argon pressure atmosphere. The molten charge was homogenized for 5 minutes after which it was poured into a MgO coated, steel split mold to produce eight 1/2-inch diameter, 8 inch long pins.

The as-cast pins were cleaned as outlined by Gangloff (14) and then controlled in 9/16 inch I.D. 95.5 percent pure aluminum oxide thermocouple tubes under a vacuum purged, positive argon pressure at growth rates of 4.7 cm/hr, 2.0 cm/hr, and .8 cm/hr. Solidification of the as-cast pins was performed in a vertical induction coil inside a vacuum chamber using the same techniques employed by Gangloff and Hoover. To obtain a better aligned structure, a water-cooled chuck was designed during the current investigation in an attempt to produce an increased thermal gradient. A schematic diagram of the water-cooled chuck is shown in Figure 24. The flow of water through the two concentric copper tubes and against the plug at the base of the small support pin removes the heat more rapidly from the ingot resulting in an increased thermal gradient.

## Heat Treatment

Disc-shaped samples, approximately 1/4-inch thick, were cut from an ingot grown at .8 cm/hr, placed in a heat treating stainless steel package, and subjected to various thermal treatments. Aging of two as-controlled specimens was carried out for 3 hours and 10 hours at 1000°C followed by a water quench. Solution treatment of the discs was performed at 1220°C for 1 hour followed by a water quench. Samples in the solution treated and quenched condition were aged for 1 hour and 100 hours at 1000°C and again quenched in water. 1/4-inch thick discs from ingots grown at 2 cm/hr (employing the water-cooled chuck) and 4.7 cm/hr were also solution treated at 1220°C for 1 hour, quenched in water, and aged for 1 hour at 1000°C.

Entire ingots were given the same age hardening treatment as described above in an attempt to produce precipitation hardened, unidirectionally solidified Ni-$Ni_3Nb$ eutectic composite fatigue specimens. However, metallographic examination of these ingots revealed the absence of $\delta$ phase precipitation within the $\gamma$ matrix. Test results revealed the severity of the quench from the solution treating temperature to be extremely important in determining the composition of the $\gamma$ matrix since the diffusion path to the $\gamma/\delta$ interface is only of the order of microns. Thus, a more severe quench was required in order to create a greater supersaturation of Nb atoms in the $\gamma$ phase. A precipitation strengthened matrix was obtained when the ingots were solution treated at 1220°C for 3 hours in an air environment, quenched in a 10% brine solution, and aged for 2 hours at 1000°C. This thermal cycle did produce $\delta$ phase precipitation of Widmanstatten morphology

within the γ matrix; however, the severity of the 10% brine quench resulted in quench cracks occurring along the lamellar interphase boundaries in some regions.

Metallographic Techniques

Metallographic specimens were wet ground through 600 grit paper, rough polished with 6 μ and 1 μ diamond paste, and final polished with a Linde B slurry. For excellent contrast between the γ and δ phases, specimens were immersion etched from 4 to 8 seconds in a Modified Marbles Reagent (Etchant A: 20 g $CuSO_4$, 200 ml ethanol, 100 ml HCl (conc.) and 100 ml $H_2O$), and viewed under both white and polarized light. Most of the photomicrographs illustrated in this thesis were obtained from samples etched with this solution. A drawback of this etch was its inability to reveal the twinning present with the δ phase.

To reveal the δ phase twins, metallographic specimens were immersion etched for 1 minute in a solution of 35 ml $HNO_3$, 2 ml HF, and 63 ml $H_2O$ (designated as Etchant B). Figures 22a and 22b, which illustrate δ phase twinning, were obtained from a fatigue specimen etched with this solution. Because the effectiveness of the etch decreased in a short period of time, it was necessary to prepare the solution immediately before etching the sample.

All fatigue fractures were nickel plated in a manner analogous to that outlined by Hill (28) to keep the fracture profile intact during metallographic preparation.

## Electron Microscopy Techniques

In order to study the fatigue mechanisms operating in the Ni-Ni3Nb composite, electron microscope replicas were made from appropriate fracture surfaces. Standard two-stage carbon replicas, shadowed parallel to the direction of crack propagation with a Pt-C mixture, were cut into small strips approximately 1 mm wide. Extreme care was taken in measuring the distance from the crack origin to each replica in an effort to relate the features found on the fracture surface to a corresponding growth rate and $\Delta K$ level.

Surface replicas were prepared from samples solution treated and aged for 1 hour and 100 hours in order to determine the percent of $\delta$ phase precipitation present. The surface of each sample was given the standard metallographic polish (described in Appendix 1: Metallographic Techniques), and was lightly etched with the Modified Marbles Reagent. A dissolved Faxfilm slurry was spread evenly over the polished surface and allowed to completely harden after which it was stripped off. A standard two-stage replica using Pt-C shadowing material was then prepared from the polished surface.

Electron microscopy of the replicas was conducted on a RCA-EMU-3G electron microscope operated at an accelerating potential of 50 kv, and on a Philips EM300 electron microscope operated at an accelerating potential of 60 and 80 kv. A goniometer stage and a high resolution stage were employed on the Philips EM300.

## Quantitative Metallography

In order to investigate the effect of heat treatment on the

amount of δ phase present, quantitative metallography was performed on samples grown at .8 cm/hour in the as-grown, solution treated and quenched, and solution treated, quenched and aged (for 1 hour and 100 hours) conditions. Point counts were conducted on polished samples viewed in an optical metallograph at a magnification of 400X. A nine-point grid was placed on the polished surface of each specimen approximately 500 times in a systematic manner such that the entire cross section of the sample was uniformly covered. For each placement of the grid, the number of grid points falling on the δ phase lamellae were recorded. Note that grid points falling on the δ precipitates in the age hardened γ matrix were not counted. The volume percent of the δ lamellae was determined by dividing the total number of grid points falling on the reinforcing δ lamellae by the total number of points counted (9 x number of grid placements). The standard error and 95 percent confidence interval for each reported volume percent were calculated using common statistical techniques (57,58).

In order to ascertain the amount of δ phase precipitation present after aging for 1 hour and 100 hours, point counts were conducted on electron micrographs taken of replicas made from polished samples that had been solution treated and aged (replication methods were discussed in the previous section). For a given sample, between fifteen and twenty different regions containing typical γ lamellae were photographed at 2200X or 3300X. These electron micrographs were enlarged into 8" x 10" pictures on which the point counts were conducted. On each photograph a twenty-five-point grid was placed exclusively over

the γ lamellae approximately 100 times in a systematic manner such that the entire matrix was uniformly covered. For each placement of the grid, the number of points falling on the δ phase precipitates were recorded. The volume percent of δ phase precipitation within the γ matrix was calculated by dividing the number of grid points falling on the δ phase precipitates by the total number of points counted (25 x number of grid placements). By knowing the volume percent of δ phase precipitation within the γ phase, and the total volume percent of γ matrix (from previous quantitative metallography), the volume percent of δ phase precipitation within the entire structure was calculated and reported.

Micro-Hardness Testing

In an attempt to investigate the effect of heat treatment on the mechanical properties of the Ni-$Ni_3Nb$ eutectic composite, micro-hardness testing was performed on the same polished samples studied during the quantitative metallography investigation. Ten Diamond Pyramid Hardness Numbers were obtained from each sample on a Tukon Micro-Hardness Tester by employing a 136° Diamond Pyramid Indenter and a 1 kilogram load. Both diagonals of the indentation were measured, averaged, and substituted into the following equation to yield the Diamond Pyramid Hardness:

$$DPH = \frac{2\ L \sin \frac{a}{2}}{d^2}$$

where L = load in kilograms applied to the indenter (1 Kg)

a = 136° apex angle

d = average length of diagonals measured in millimeters.

The standard deviation for the data obtained was calculated using common statistical techniques (59).

# VITA

William J. Mills was born the son of John P. and Margery (Siegman) Mills in Montgomery, New York. He received his elementary and secondary education from the Valley Central (Montgomery, New York) School System and was graduated from Valley Central High School in 1967.

In June, 1971, Mr. Mills was graduated with Honors from Lehigh University with a degree of Bachelor of Science in Metallurgy and Materials Science. Upon completion of his undergraduate studies, the author continued his education as a research assistant working under Dr. R. W. Hertzberg and Dr. R. W. Kraft on a NASA research grant number NGR-39-007-007. He was appointed an Instructor in the Department of Metallurgy and Materials Science in January, 1972. Mr. Mills presented a paper entitled "Fatigue Crack Propagation of the Ni-$Ni_3Nb$ Eutectic Composite" at the 1973 Spring Meeting of the Metallurgical Society of the AIME. The author plans to continue his education towards the Ph.D. degree in Metallurgy at Lehigh University.